Luminescence of Lanthanide Complexes with Perfluorinated Alkoxide Ligands

Christopher M. Kotyk,[a] Jeremy E. Weber,[b] Ariel S. Hyre,[c] James McNeely,[c] Jorge H. S. K. Monteiro,[d] Marek Domin,[e] Gary J. Balaich,[g] Arnold L. Rheingold,[f] Ana de Bettencourt-Dias,[h] Linda H. Doerrer[c]*

[a]Department of Chemistry, Wheaton College, Norton, MA 02766, USA

[b]Department of Chemistry, Yale University, New Haven, CT 06520, USA

[c]Department of Chemistry, Boston University, Boston, MA 02215, USA

[d]Department of Chemistry, Humboldt State University, Arcata, CA 95521, USA

[e]Department of Chemistry, Merkert Chemistry Center, Boston College, Chestnut Hill, MA 02467, USA

[f]Department of Chemistry, University of California, San Diego, La Jolla, CA 92093, USA

[g]Department of Chemistry, United States Air Force Academy, United States Air Force Academy, CO 80840, USA

[h]Department of Chemistry, University of Nevada, Reno, NV 89557, USA

ABSTRACT

Four groups of rare earth complexes, comprising eleven new compounds, with fluorinated O-donor ligands ([K(THF)$_6$][Ln(OC$_4$F$_9$)$_4$(THF)$_2$], **1-Ln** (Ln = Ce, Nd), [K][Ln(OC$_4$F$_9$)$_4$], **2-Ln** (Ln = Eu, Gd, Dy), [K(THF)$_2$][Ln(pin^F)$_2$(THF)$_3$], **3-Ln** (Ln = Ce, Nd), and [K(THF)$_2$][Ln(pin^F)$_2$(THF)$_2$], **4-Ln** (Ln = Eu, Gd, Dy, Y) have been synthesized and characterized. Single-crystal X-ray diffraction data were collected for all compounds except **2-Ln**. Species **1-Ln**, **3-Ln**, and **4-Ln** are uncommon examples of six- (Eu, Gd, Dy, Y) and seven- (Ce, Nd) coordinate Ln^{III} centers in all-oxygen-donor environments. Species **1-Ln**, **2-Ln**, **3-Ln**, and **4-Ln** are all luminescent (except where Ln = Gd, Y) with the solid-state emission of **1-Ce** being exceptionally blue-shifted for a cerium complex. The emission spectra of the six Nd, Eu, and Dy complexes do not show large differences based on ligand and are generally consistent with the well-known free-ion spectra. Time-dependent DFT results show that **1-Ce** and **3-Ce** undergo allowed $5f \rightarrow 4d$ excitations, consistent with luminescence lifetime measurements in the nanosecond range. Europium-containing **2-Eu** and **4-Eu**, however, were found to have luminescence lifetimes in the millisecond range, indicating phosphorescence rather than fluorescence. The performance of a pair of multi-reference models for the prediction of the Ln = Nd, Eu, Dy absorption spectra was assessed. It was found that
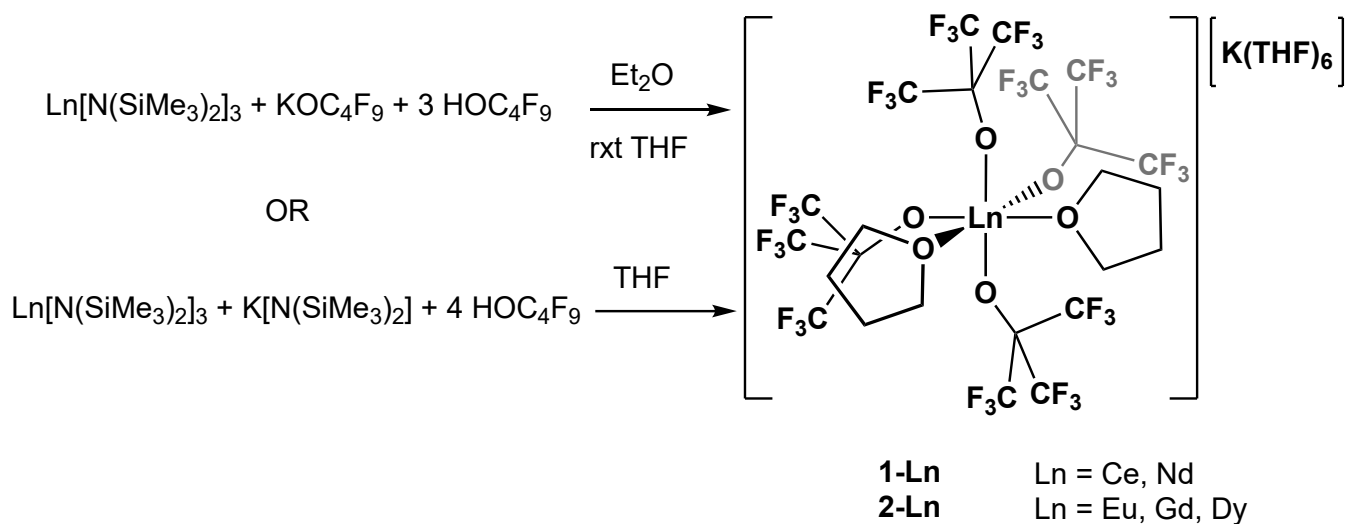
spectroscopy-oriented configuration interaction as applied to a simplified model in which the free ion lanthanide was embedded in ligand-centered Löwdin point charges performed as well (Nd) or better (Eu, Dy) than canonical NEVPT2 calculations where the ligand orbitals were included in the treatment.
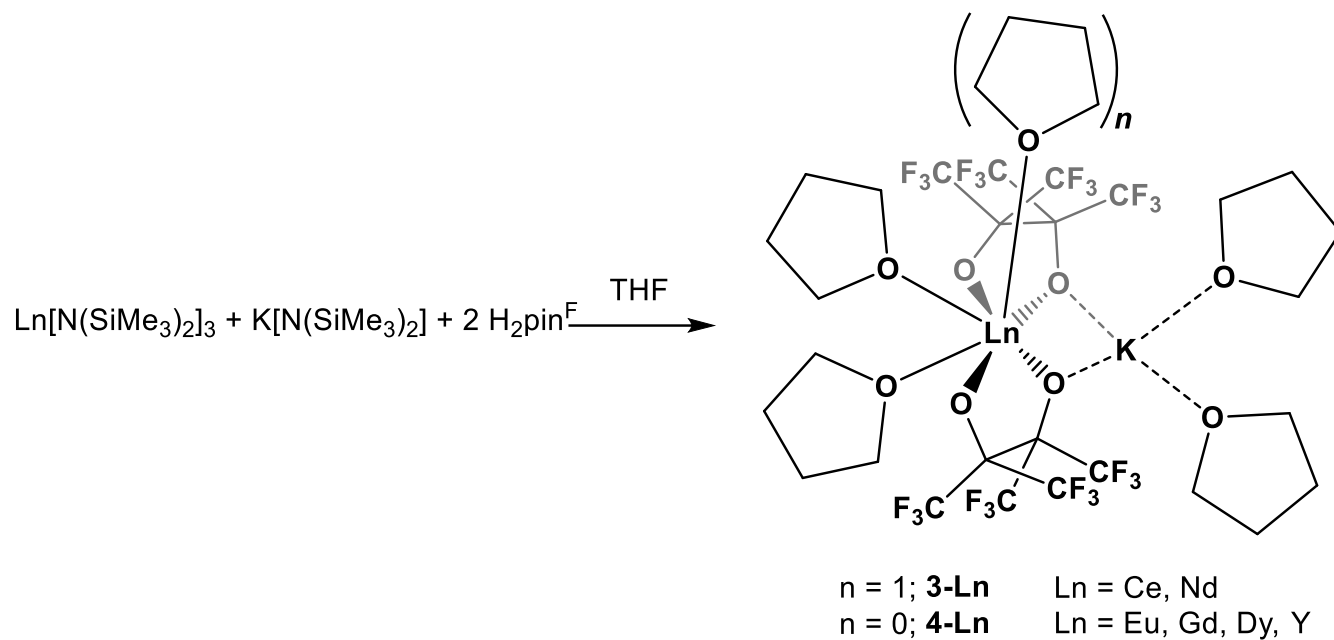
INTRODUCTION

The lanthanide (Ln^{III}) ions are well known for their magnetism and photophysical properties, and are used in lasers, consumer electronics, medical contrast agents, and many other applications.[1-7] Lanthanide compounds in which structure-property relationships are elucidated are important precursors to these materials. Like other strongly Lewis-acidic rare earth metals, cerium has a strong affinity for hard Lewis bases, such that oxygen donors like β-diketonates[8-13] and alkoxides[5, 14-18] have been extensively investigated. Early Ln^{III} compounds with fluorinated ligands were designed for the deposition of mixed metal oxides, as fluorination improves the volatility and thermal stability of precursors for the manufacture of thin films via chemical vapor deposition (CVD).[19-24] In addition, replacing ligand C–H bonds with C–F bonds has been shown to reduce vibrational energy loss that can quench emissions in the NIR range,[25] resulting in improved emission quantum yield. To date, however, there are fewer lanthanide complexes with fluorinated ligands than without. Therefore, new Ln-containing complexes with fluorinated ligands have the potential to be useful and informative for their differences from the corresponding proteo analogs.

Our group has previously used fluorinated alkoxides and aryloxides to produce a family[26] of complexes including an unusual trivalent Cu[27] species, three-coordinate transition metal complexes in exclusively O-donor environments,[28] and rare high-spin square-planar metal centers.[26, 29] To date, five $3d$ metals (Fe,[28-30] Co,[28, 31] Ni,[32] Cu,[27-28, 31, 33-35] Zn[28, 36]) have been prepared as homonuclear, homoleptic $[M(pin^F)_2]^{2-}$ and $[M(OC_4F_9)_n]^{m-}$ complexes, heteroleptic $[(R_3P)_2M(OR^F)_2]$ complexes,[37] as well as the main group species $Tl(OC_4F_9)$[31]. Thus, with the goal of preparing luminescent Ln^{III} complexes with fluorinated alkoxide ligands and homoleptic O-donor environments, we undertook the synthesis and characterization of a series of Ln^{III} complexes, whose results are shown in Scheme 1, with $[OC_4F_9]^-$ ligands, and in Scheme 2 for $[pin^F]^{2-}$ (perfluoropinacolate) ligands. The compounds may be grouped in four categories based on ligand and coordination number: ($[K(THF)_6][Ln(OC_4F_9)_4(THF)_2]$, **1-Ln** (Ln = Ce, Nd), $[K][Ln(OC_4F_9)_4]$, **2-Ln** (Ln = Eu, Gd, Dy), $[K(THF)_2][Ln(pin^F)_2(THF)_3]$, **3-Ln** (Ln = Ce, Nd), and $[K(THF)_2][Ln(pin^F)_2(THF)_2]$, **4-Ln** (Ln = Eu, Gd, Dy, Y).

Ln[N(SiMe$_3$)$_2$]$_3$ + KOC$_4$F$_9$ + 3 HOC$_4$F$_9$ $\xrightarrow[\text{rxt THF}]{\text{Et}_2\text{O}}$

OR

Ln[N(SiMe$_3$)$_2$]$_3$ + K[N(SiMe$_3$)$_2$] + 4 HOC$_4$F$_9$ $\xrightarrow{\text{THF}}$

F$_3$C CF$_3$
F$_3$C CF$_3$
F$_3$C
CF$_3$
O
O
F$_3$C
F$_3$C
O—Ln—O
O
F$_3$C
O
CF$_3$
F$_3$C CF$_3$
[K(THF)$_6$]

1-Ln   Ln = Ce, Nd
2-Ln   Ln = Eu, Gd, Dy

Scheme 1. Syntheses of the **1-Ln** and **2-Ln** families with the OC$_4$F$_9$ ligand.

Ln[N(SiMe$_3$)$_2$]$_3$ + K[N(SiMe$_3$)$_2$] + 2 H$_2$pin^F $\xrightarrow{\text{THF}}$

F$_3$CF$_3$C CF$_3$ CF$_3$
O
O O
Ln
O O
K
O O
O
F$_3$C F$_3$C CF$_3$ CF$_3$

n = 1; **3-Ln**   Ln = Ce, Nd
n = 0; **4-Ln**   Ln = Eu, Gd, Dy, Y

Scheme 2. Syntheses of the **3-Ln** and **4-Ln** families with the pin^F ligand.

EXPERIMENTAL

General procedures.

All syntheses described below were conducted in an inert and anhydrous atmosphere using standard Schlenk line and glovebox techniques at room temperature. The anhydrous solvents THF, Et_2O, and hexanes were dried in an alumina-based solvent purification system (SPS) under Ar, piped directly into a N_2-filled MBraun drybox, and stored over molecular sieves. Potassium hydride (KH) was obtained as a mineral oil dispersion (30 wt %) and purified by washing with hexanes and drying in vacuo prior to storage in a glovebox. The alcohols H_2pin^F and HOC_4F_9 were purchased from Oakwood Chemical, dried over molecular sieves, degassed by three freeze-pump-thaw cycles, and vacuum-transferred prior to use. Toluene and dimethoxyethane (DME) were dried by refluxing over Na/benzophenone under an N_2 atmosphere and distilled. Acetonitrile was distilled from CaH_2 under N_2. Celite (Aldrich) was heated to 125°C under vacuum overnight and stored under N_2. $KN(SiMe_3)_2$ was purchased from Aldrich, dissolved in toluene, filtered through Celite, and dried under reduced pressure before use. Anhydrous $LnCl_3$ (Ln = Ce, Nd, Eu, Dy, Y) salts were purchased from Strem and used as received. Anhydrous $Ln[N(SiMe_3)_2]_3$ (Ln = Ce, Nd, Eu, Dy, Y) were prepared according to the literature.[38] UV-vis data were collected with a Shimadzu UV-3600 spectrometer. Elemental analyses were performed by Atlantic Microlabs, Inc. (Norcross, Georgia). Mass Spectrometry data were collected with a Voyager DE STR (MALDI), using a nitrogen laser with DCTB as the matrix.

Synthetic procedures.

[K(THF)₆][Ce(OC₄F₉)₄(THF)₂], 1-Ce. A solution of HOC_4F_9 (61 μL, 0.44 mmol) in Et_2O (3 mL) was added to a stirred yellow solution of $Ce[N(SiMe_3)_2]_3$ (91 mg, 0.15 mmol) in Et_2O (3 mL), causing a color change to colorless. A solution of KOC_4F_9 (41 mg, 0.15 mmol) in Et_2O (3 mL) was added to the stirred solution. After 1 hour, the solvent was removed under vacuum and the resulting solids were dissolved in minimal THF, filtered into a vial, and chilled at −35 °C for an hour. The solution was layered with room temperature hexane and stored at −35 °C producing crystals over 7 days (64 mg, 26%). Colorless X-ray quality crystals were grown over 2 days in minimal THF layered with 1:2 THF:hexane at −35 °C. ESI-MS: m/z calcd for $[Ce(OC_4F_9)_4]^-$ 1080.23, found 1080. Solution-state maxima: absorption, 298 nm; emission, 406 nm. Solid-state maxima: excitation, 275 nm; emission, 357 nm. Solid-state maxima: excitation, 256 nm; emission, 356 nm.

[K(THF)$_6$][Nd(OC$_4$F$_9$)$_4$(THF)$_2$], 1-Nd. HOC$_4$F$_9$ (425 µL, 3.05 mmol) was added dropwise to a stirred blue solution of Nd[N(SiMe$_3$)$_2$]$_3$ (625 mg, 0.999 mmol) in Et$_2$O (5 mL), causing a color change to light blue. KOC$_4$F$_9$ (266 mg, 0.962 mmol) was added and was stirred overnight. The solvent was removed under vacuum and the resulting solids were dissolved in minimal THF, filtered into a vial, layered with hexane and stored at −35 °C. Dichroic blue/pink X-ray quality crystals were grown over 2 days at −35 °C (500 mg, 31 %). ESI-MS: m/z calcd for [Nd(OC$_4$F$_9$)$_4$]$^-$ 1084.36, found 1084. Solid-state maxima: excitation, 350 nm, 525 nm, 580 nm.

[K][Eu(OC$_4$F$_9$)$_4$], 2-Eu. A solution of KOC$_4$F$_9$ (43 mg, 0.16 mmol) in THF (3 mL) was added to a stirred orange solution of Eu[N(SiMe$_3$)$_2$]$_3$ (98 mg, 0.16 mmol) in THF (3 mL), causing a color change to yellow. HOC$_4$F$_9$ (65 µL, 0.47 mmol) was added in 10 µL aliquots using a 10 µL graduated glass syringe causing a color change to colorless and was stirred overnight. The solvent was removed under vacuum and the resulting solids were dissolved in minimal THF, filtered into a vial, and chilled at −35 °C for an hour. The solution was layered with room temperature hexane and stored at −35 °C producing colorless crystals over 4 days (157 mg, 59 %). ESI-MS: m/z calcd for [^{151}Eu(OC$_4$F$_9$)$_4$]$^-$ 1090.84, found 1091; calcd for [^{153}Eu(OC$_4$F$_9$)$_4$]$^-$ 1092.84, found 1093. Solid-state maxima: excitation, 263 nm; emission, 611 nm.

[K][Gd(OC$_4$F$_9$)$_4$], 2-Gd. A solution of KN(SiMe$_3$)$_2$ (39 mg, 0.20 mmol) in THF (2 mL) was added to a stirred colorless solution of Gd[N(SiMe$_3$)$_2$]$_3$ (125 mg, 0.196 mmol) in THF (4 mL). HOC$_4$F$_9$ (110 µL, 0.788 mmol) was added using a 25 µL graduated glass syringe. After 10 minutes, the solvent was removed under vacuum and the resulting solids were dissolved in minimal THF, filtered into a vial, and chilled at −35 °C for two hours. The solution was layered with room temperature hexane and stored at −35 °C producing colorless crystals over 3 days, which were recrystallized from a chilled THF solution layered with room temperature hexane at −35 °C over 5 days. ESI-MS: m/z calcd for [^{158}Gd(OC$_4$F$_9$)$_4$]$^-$ 1097.85, found 1098; [^{155}Gd(OC$_4$F$_9$)$_4$]$^-$ 1094.85, found 1095.

[K][Dy(OC$_4$F$_9$)$_4$], 2-Dy. A solution of KOC$_4$F$_9$ (43 mg, 0.16 mmol) in Et$_2$O (5 mL) was added to a stirred colorless solution of Dy[N(SiMe$_3$)$_2$]$_3$ (101 mg, 0.157 mmol) in Et$_2$O (5 mL), causing no color change. HOC$_4$F$_9$ (66 µL, 0.47 mmol) in Et$_2$O (5 mL) was added dropwise and was allowed to stir at room temperature. After 4 days, the solvent was removed under vacuum and the resulting solids were dissolved in minimal THF, filtered into a vial, and chilled at −35 °C for an hour. The solution was layered with room temperature hexane and stored at −35 °C producing colorless crystals over 6 days (105 mg, 39 %). ESI-MS: m/z calcd for [^{160}Dy(OC$_4$F$_9$)$_4$]$^-$ 1099.85, found 1100; [^{161}Dy(OC$_4$F$_9$)$_4$]$^-$ 1100.85, found 1101;

[^{162}Dy(OC$_4$F$_9$)$_4$]$^-$ 1101.85, found 1102; [^{163}Dy(OC$_4$F$_9$)$_4$]$^-$ 1102.85, found 1103; [^{164}Dy(OC$_4$F$_9$)$_4$]$^-$ 1103.85, found 1104. Solid-state maxima: excitation, 298 nm, 324 nm, 350 nm, 364 nm, 378 – 404nm.

[K(THF)$_2$][Ce(pin^F)$_2$(THF)$_3$], 3-Ce. A solution of KN(SiMe$_3$)$_2$ (160 mg, 0.802 mmol) and H$_2$pin^F (287 µL, 1.61 mmol) in THF (5 mL) was added to a stirred yellow solution of Ce[N(SiMe$_3$)$_2$]$_3$ (500 mg, 0.805 mmol) in THF (5 mL), causing a color change to amber, and was stirred overnight. The solvent was removed under vacuum and the resulting solids were dissolved in minimal THF, filtered into a vial, layered with hexane and stored at −35 °C. Pale orange X-ray quality crystals were grown over 5 days at −35 °C (459 mg, 47 %). ESI-MS: m/z calcd for {[K][Ce(pin^F)$_2$]$_2$}$^-$ 1647.51, found 1647. Solution-state maxima: absorption, 248 nm, 322 nm; emission, 452 nm. Solid-state maxima: excitation, 281 nm; emission, 405 nm. Solid-state maxima: excitation, 265 nm; emission, 405 nm.

[K(THF)$_2$][Nd(pin^F)$_2$(THF)$_3$], 3-Nd. A solution of KN(SiMe$_3$)$_2$ (160 mg, 0.802 mmol) and H$_2$pin^F (290 µL, 1.62 mmol) in THF (5 mL) was added to a stirred blue solution of Nd[N(SiMe$_3$)$_2$]$_3$ (499.7 mg, 0.7995 mmol) in THF (5 mL), causing a color change to yellow, and was stirred overnight. The solvent was removed under vacuum and the resulting solids were dissolved in minimal THF, filtered into a vial, layered with hexane and stored at −35 °C. Colorless crystals were grown over 4 days at −35 °C. X-ray quality crystals were grown over 2 days in minimal THF layered with hexane at −35 °C (428 mg, 44 %). ESI-MS: m/z calcd for {[K][Nd(pin^F)$_2$]$_2$}$^-$ 1655.76, found 1655. Solid-state maxima: excitation, 350 nm, 525 nm, 580 nm.

[K(THF)$_2$][Eu(pin^F)$_2$(THF)$_2$], 4-Eu. A solution of KN(SiMe$_3$)$_2$ (70 mg, 0.35 mmol) in THF (5 mL) was added to a stirred orange solution of Eu[N(SiMe$_3$)$_2$]$_3$ (216 mg, 0.341 mmol) in THF (10 mL). The solution was stirred for 5 min, during which time it turned deep green. A solution of H$_2$pin^F (121 µL, 0.680 mmol) in THF (5 mL) was added to the reaction mixture, causing an immediate color change to clear and colorless with a slight yellow tint, and was stirred overnight. The solvent was removed under vacuum and the resulting solids were dissolved in minimal THF, filtered into a vial, and chilled at −35 °C for an hour. The solution was layered with room temperature hexane and stored at −35 °C producing colorless crystals overnight (149 mg, 38 %). X-ray quality crystals were grown by vapor diffusion in concentrated THF against hexane at room temperature over 6 days. ESI-MS: m/z calcd for {[K]$_3$[^{151}Eu(pin^F)$_2$]}$^+$ 1746.61, found 1747; {[K]$_3$[^{151}Eu(pin^F)$_2$][^{153}Eu(pin^F)$_2$]$^+$} 1748.61, found 1749; {[K]$_3$[^{153}Eu(pin^F)$_2$]}$^+$ 1750.62, found 1751; {[K][^{151}Eu(pin^F)$_2$]$_2$[^{153}Eu]$^{2+}$} 1821.61: found 1822; {[K][^{153}Eu(pin^F)$_2$][^{151}Eu(pin^F)$_2$][^{153}Eu]$^{2+}$} 1823.61, found 1824; {[K][^{153}Eu(pin^F)$_2$]$_2$[^{153}Eu]$^{2+}$} 1825.61, found 1826. Solid-state maxima: excitation, 464 nm; emission 618 nm.

[K(THF)₂][Gd(pinᶠ)₂(THF)₂], 4-Gd. A solution of KN(SiMe₃)₂ (80 mg, 0.40 mmol) in THF (3 mL) was added to a stirred colorless solution of Gd[N(SiMe₃)₂]₃ (248 mg, 0.388 mmol) in THF (5 mL). H₂pinᶠ (140 μL, 0.784 mmol) was added using a 25 μL graduated glass syringe. After 60 minutes, the solvent was removed under vacuum and the resulting solids were dissolved in minimal THF, filtered into a vial, and chilled at −35 °C for an hour. The solution was layered with room temperature hexane and stored at −35 °C producing tinted crystals overnight, which were recrystallized in THF layered with hexane and stored at −35 °C over 3 days to produce colorless crystals (226 mg, 51%). X-ray quality crystals were grown by vapor diffusion in a concentrated THF solution against hexane vapor. ESI-MS: m/z calcd for {[K][¹⁶⁰Gd(pinᶠ)₂][¹⁶⁰Gd(pinᶠ)(O)₂]³⁻} 1386.7, found 1387; {[K][¹⁵⁷Gd(pinᶠ)₂]₂⁻} 1680.7, found 1681; {[K][¹⁵⁶Gd(pinᶠ)₂][¹⁵⁸Gd(pinᶠ)₂]⁻} 1680.7, found 1681; {[K][¹⁵⁷Gd(pinᶠ)₂][¹⁵⁸Gd(pinᶠ)₂]⁻} 1681.7, found 1682; {[K][¹⁵⁸Gd(pinᶠ)₂]₂⁻} 1682.7, found 1683; {[K][¹⁵⁶Gd(pinᶠ)₂][¹⁶⁰Gd(pinᶠ)₂]⁻} 1682.7, found 1683; {[K][¹⁵⁷Gd(pinᶠ)₂][¹⁶⁰Gd(pinᶠ)₂]⁻} 1683.7, found 1684; {[K][¹⁵⁸Gd(pinᶠ)₂][¹⁶⁰Gd(pinᶠ)₂]⁻} 1684.7, found 1685.

[K(THF)₂][Dy(pinᶠ)₂(THF)₂], 4-Dy. A solution of KN(SiMe₃)₂ (35 mg, 0.18 mmol) in THF (5 mL) was added to a stirred colorless solution of Dy[N(SiMe₃)₂]₃ (112 mg, 0.174 mmol) in THF (5 mL). H₂pinᶠ (62 μL, 0.35 mmol) was added in 10 μL aliquots using a 10 μL graduated glass syringe, causing a slight yellow tint, and was stirred overnight. The solvent was removed under vacuum and the resulting solids were dissolved in minimal THF, filtered into a vial, and chilled at −35 °C for an hour. The solution was layered with room temperature hexane and stored at −35 °C producing colorless crystals over 3 days (126 mg, 63 %). X-ray quality crystals were grown by vapor diffusion in concentrated THF against hexane at room temperature over 3 days. ESI-MS: m/z calcd for {[K]₃[¹⁶²Dy(pinᶠ)₂]₂⁺} 1768.63, found 1769; {[K]₃[¹⁶²Dy(pinᶠ)₂][¹⁶³Dy(pinᶠ)₂]⁺} 1769.63, found 1770; {[K]₃[¹⁶²Dy(pinᶠ)₂][¹⁶⁴Dy(pinᶠ)₂]⁺} 1770.63, found 1771; {[K]₃[¹⁶³Dy(pinᶠ)₂][¹⁶⁴Dy(pinᶠ)₂]⁺} 1771.63, found 1772; {[K]₃[¹⁶⁴Dy(pinᶠ)₂]₂⁺} 1772.63, found 1773. Solid-state maxima: excitation, 298 nm, 324 nm, 350 nm, 364 nm, 378 – 404nm.

[K(THF)₂][Y(pinᶠ)₂(THF)₂], 4-Y. A solution of KN(SiMe₃)₂ (77 mg, 0.39 mmol) in THF (2 mL) was added to a stirred colorless solution of Y[N(SiMe₃)₂]₃ (229 mg, 0.388 mmol) in THF (5 mL). H₂pinᶠ (140 μL, 0.784 mmol) was added in 10 μL aliquots using a 10 μL graduated glass syringe, creating a slight yellow tint. After 5 minutes, the solvent was removed under vacuum and the resulting solids were dissolved in minimal THF, filtered into a vial, and chilled at −35 °C for an hour. The solution was layered with room temperature hexane and stored at −35 °C producing colorless crystals over 7 days, which were recrystallized from minimal THF layered with hexane at −35 °C over 4 days (223 mg, 56 %). X-ray

quality crystals were grown over 9 days in minimal THF layered with hexane at −35 °C. ESI-MS: m/z calcd for $\{[K][Y(pin^F)_2]_2{}^-\}$ 1544.66, found 1545; $\{[K_2pin^F]_3[Y(pin^F)_2]^-\}$ 1982.54, found 1983.

Spectroscopy.

Electronic absorption spectra for **1-Ce**, **1-Nd**, **3-Ce**, and **3-Nd** were collected in THF with a Shimadzu UV-3600 spectrometer and quartz cuvettes. Solid-state photoluminescence data for **2-Eu, 2-Dy, 4-Eu,** and **4-Dy** were collected at 298 K, on a Fluorolog spectrofluorimeter (Horiba Jobin Yvon FL3-22-iHR550) with an excitation monochromator with 1200 grooves/mm gratings blazed at 330 nm and an emission monochromator with 1200 grooves/mm gratings blazed at 500 nm (UV-Vis) or an emission monochromator with 600 grooves/mm gratings blazed at 1000 nm (NIR). An ozone-free xenon lamp of 450 W (Ushio) was used as the radiation source. The excitation spectra, corrected for instrumental function, were measured between 250 and 600 nm. The emission spectra were measured in the range 320-1500 nm in front face mode at 22.5° for the solid-state samples. All emission spectra were corrected for instrumental function. For **1-Ce** and **3-Ce**, the emission decay curves were obtained using a TCSPC system and a Horiba NanoLED model N-265 (peak wavelength = 265 ± 10 nm, 1 − 2 pJ/pulse) as excitation source. For **2-Eu** and **4-Eu**, the emission decay curves were obtained using a TCSPC system and a pulsed Xe lamp (pulse width ~5 μs) as excitation source. Before all decay curve measurements, the spectrum of a blank, using Ludox® solution, was obtained.

Theoretical Calculations

Single-point calculations and gas-phase geometry optimizations of the ground states of all compounds (except **4-Y**) were performed at the BP86 level of theory with Gaussian16, Revision A.03.[39] The 6-31G* basis set was used for H, C, O, F, and K atoms, and all lanthanides were treated by the Stuttgart RSC ANO/ECP basis set[40] provided by Basis Set Exchange.[41-42] **4-Y** was treated with the Stuttgart RSC 1997 ECP[43] and a double-ζ valence basis set, also from the BSE. Starting coordinates for **1-Ln**, **3-Ln**, and **4-Ln** (except Ln = Y) were obtained from crystal structures. Outer-sphere counter cations were removed from OC_4F_9–containing species, such that calculations were performed on gas-phase $[Ln(OC_4F_9)_4(THF)_2]^-$ ions. Optimized coordinates for **1-Nd** were modified to be used as starting coordinates for **2-Eu** and **2-Dy**, which are assumed to be of the same six-coordinate geometry despite limited ESI-MS data that cannot observe neutral THF fragments. Final coordinates from optimized geometries are available in the supporting information. Time-dependent density functional theory (TD-

DFT) calculations at the B3LYP level of theory were performed on **1-Ce** and **3-Ce** using optimized gas-phase structures with Gaussian16. A frozen core of the inner noble gas electrons was used for cerium to reduce computational time. Additional electronic structure analyses were performed using GaussView 6,[44] ChemCraft 1.8,[45] and the NBO 6.0[46-47] package as provided in the 2016 release of the Amsterdam Density Functional (ADF) program suite.[48-49]

The absorption spectra of **1-Nd**, **2-Eu, 2-Dy**, **3-Nd**, **4-Eu**, and **4-Dy** were modeled using the ORCA package, version 4.0.[50-52] The recently released SARC2-DKH-QZVP[53] basis set was used for all Ln atoms and the relativistically recontracted DKH-DEF2-SV(P)[54] basis set was used for all other atoms. Scalar relativistic effects were accounted for with the second-order Douglas-Kroll-Hess approximation (DKH2)[55]. The absorption spectra were modeled with quasi-degenerate perturbation theory on top of strongly contracted n-electron valence perturbation theory applied to state-averaged CASSCF wavefunctions (QDPT+NEVPT2/SA-CASSCF),[56] which has been successfully applied to Ln^{III} systems by Neese et al.[53, 57] The active space for the SA-CASSCF calculations included 3/6/9 electrons correlated with 7 f-orbitals for the Nd/Eu/Dy species. For the Nd species (**1-Nd**, **3-Nd**), the active space was averaged over the full set of states derived from the free ion terms (35 quartet, 112 doublet [QDPT+SA(35,112)-NEVPT2(3,7)]) for a complete intermediate coupling treatment. For the Eu species (**2-Eu**, **4-Eu**), the active space was averaged over the states derived from the full set of septet and quintet free ion states, and triplet states derived from the ^{3}P, ^{3}O, ^{3}M, ^{3}K, ^{3}H, ^{3}F, and ^{3}I free ion states (7 septet, 140 quintet, 91 triplet [QDPT+SA(7,140,91)-NEVPT2(6,7)]). We have also averaged over the ^{7}F, ^{5}D, ^{5}L, ^{5}G, ^{5}H, ^{5}F, ^{5}I, and ^{3}P free ion terms (7 septet, 62 quintet, 3 triplet [QDPT+SA(7,62,3)-NEVPT2(6,7)]) as suggested by Freidzon et al.,[58] for benchmarking purposes. For the Dy species (**2-Dy**, **4-Dy**), the active space was averaged over the states derived from ^{6}H, ^{6}F, ^{6}P, ^{4}F(1), ^{4}G(1), ^{4}I(1), ^{4}M, ^{4}K, ^{4}L, ^{4}P, ^{4}D(1), ^{4}I(2), ^{4}D(2), ^{4}H, ^{4}G(2), ^{4}F(2), ^{2}L, ^{2}K, ^{2}P, ^{2}N, ^{2}F, ^{2}M, ^{2}H, and ^{2}D free ion terms (21 sextet, 133 quartet, 98 doublet [QDPT+SA(21,133,98)-NEVPT2(9,7)]). We have also averaged over the ^{6}H, ^{6}F, ^{6}P, ^{4}F, ^{4}G, ^{4}I, ^{4}M, ^{4}K, and ^{4}L free ion terms as suggested by Freidzon et al.,[58] (QDPT+SA(21,80)-NEVPT2(9,7)). Spin-orbit coupling was included with quasi-degenerate perturbation theory (QDPT) using the SA-CASSCF wavefunction and strongly contracted NEVPT2[59-61] diagonal energies. Relativistic picture change effects were included for the spin-orbit mean field operator.

To both estimate the effect of ligand-metal orbital interactions on the energy levels of **1-Nd**, **3-Nd**, **2-Eu,**, **4-Eu**, **2-Dy**, and **4-Dy** and to perhaps improve on the NEVPT2 results described above, trivalent Nd/Eu/Dy ions were embedded in a field of atom-centered Löwdin point charges obtained from PBE0/DEF2-SVP/DKH calculations performed on the tetraanionic (four OC$_4$F$_9$ ligands in **1-Nd, 2-Eu,**

2-Dy) or trianionic ligand (two pin^F and one K^+ in **3-Nd**, **4-Eu, 4-Dy**) combinations from the optimized geometries. The embedded free ions were then modeled with quasi-degenerate perturbation theory on top of spectroscopy-oriented configuration interaction[62] based on state-averaged CASSCF references (QDPT+SORCI^{emb}/SA-CASSCF^{emb}). Finally, we again note here that the theoretical models listed above were used to predict absorption spectra, not excitation spectra. While we would not expect the differences between the absorption and emission spectra to be significant at higher wavelengths, there might be a greater intensity at shorter wavelengths in the absorption spectra due to non-radiative relaxation processes upon emission.

NBO calculations were based on B3LYP/DKH/SARC2-DKH-QZVP[Ln]/DKH-DEF2-SV(P) [H,C,O,F, K]/cc-pVTZ-DK[63](Y) electron densitites.

RESULTS AND DISCUSSION

Synthesis

The $[\text{Ln}(\text{OC}_4\text{F}_9)_4]^-$ compounds, Scheme 1, are prepared from $\text{Ln}[\text{N}(\text{SiMe}_3)_2]_3$ with three equivalents of HOC_4F_9 in the presence of a base, which can be either $\text{KN}(\text{SiMe}_3)_2$ or KOC_4F_9, in either Et_2O or THF. X-ray quality single crystals of $[\text{Ln}(\text{OC}_4\text{F}_9)_4]^-$ (**1-Ce**, **1-Nd**) are readily isolated from a concentrated, cold solution of THF layered with hexane or a hexane/THF blend. Crystalline material can be obtained for the analogous compounds with smaller rare earth metals, $[\text{Ln}(\text{OC}_4\text{F}_9)_4]^-$ (**2-Eu**, **2-Gd**, **2-Dy**), although robust X-ray quality single crystals could not be obtained. The $[\text{Ln}(\text{pin}^F)_2]^-$ compounds (**3-Ln**, **4-Ln**), Scheme 2, are all prepared from $\text{Ln}[\text{N}(\text{SiMe}_3)_2]_3$ in the presence of $\text{KN}(\text{SiMe}_3)_2$ in THF. These compounds are initially purified by recrystallization from a concentrated, cold solution of THF layered with hexane. X-ray quality single crystals can be obtained either from this method (**3-Ce**, **3-Nd**, **4-Y**), or at room temperature by vapor diffusion into concentrated THF of a hexane countersolvent (**4-Eu**, **4-Gd**, **4-Dy**).

Solution Behavior

Rare earth complexes of the fluorinated ligands $[\text{OC}_4\text{F}_9]^-$ and $[\text{pin}^F]^{2-}$ are water-sensitive (pKa$_1$ values of 10.7 and 6.05 respectively). Although transition metal $[\text{M}(\text{pin}^F)_2]^{2-}$ complexes can be air stable, and even soluble in water, all the complexes reported herein are sensitive to water, perhaps due to the lability of THF and ease of its replacement with H_2O, which could lead to protonolysis and Ln_2O_3 formation. Ce^{III}-containing **1-Ce** and **3-Ce** are also air-sensitive and susceptible to oxidation due to the ease of forming CeO_2.

Solid-State Structures.

Structural data for the monodentate $[OC_4F_9]^{1-}$-containing complexes $[Ln(OC_4F_9)_4(THF)_2]^-$, **1-Ln** (Ln = Ce, Nd) are compared in Table 1, and data collection parameters are given in Table S1. Compounds **1-Ce** and **1-Nd** are monoanionic and are accompanied by a THF-coordinated potassium countercation, $[K(THF)_6]^+$, in the outer sphere (Figure 1). Compound **1-Ce** is six-coordinate at Ce and the four Ce–O(OC_4F_9) bonds have two distinct lengths: those *trans* to the THFs, Ce(1)–O(2), have bond distances of 2.275(4) Å, while those *trans* to each other, Ce(1)–O(1), are slightly longer at 2.296(3) Å (Scheme 3, Table 1). These values are consistent with the literature in which Ce–O distances range from 2.208 Å[64] to 2.652 Å,[17] with a mean of 2.3(1) Å.[17, 64-70] The THF ligands are *cis* to each other and identical by symmetry, with a Ce(1)–O(3) bond length of 2.587(4) Å. The same features are seen in **1-Nd**, which maintains the same six-coordinate geometry as shown in Figure S1. The Nd(1)–O(1) bond distances, 2.272(5) Å, are longer than Nd(1)–O(2), 2.242(5) Å, while Nd(1)–O(3) has the longest distance, 2.558(6) Å.

Table 1. Selected distances (Å) and angles (°) in crystal structures of **1-Ce** and **1-Nd**.

	1-Ce	1-Nd
Ln(1)–O(1)[a]	2.296(3)	2.272(5)
Ln(1)–O(2)[a]	2.275(4)	2.242(5)
Ln(1)–O(3)[b]	2.587(4)	2.558(6)
O(1)–Ln(1)–O(2)	93.73(17)	93.9(2)
O(1)–Ln(1)–O(2)	97.96(17)	98.1(2)
O(1)–Ln(1)–O(3)	81.81(14)	81.2(2)
O(1)–Ln(1)–O(3)	82.94(14)	83.3(2)
O(2)–Ln(1)–O(3)	87.60(15)	88.4(2)
O(2)–Ln(1)–O(3)	165.40(15)	165.9(2)

[a]O(1) and O(2) are oxygen atoms from $[OC_4F_9]^-$

[c]O(3) are oxygen atoms from THF

Although no X-ray diffraction quality crystals were obtained for the $[OC_4F_9]^-$ complexes **2-Ln** (Ln = Eu, Gd, Dy), ESI-MS data are consistent with the assigned formulae for all. Based upon photoluminescence data (*vide infra*) and the scarcity of non-polymeric four-coordinate complexes of Eu,[71-89] Gd,[82, 90-96] and Dy[82, 89, 97-108] in the literature, it is proposed that **2-Ln** also bear two THF ligands as seen in **1-Ln** such that the solution structures are six-coordinate. In the absence of crystallographic data for **2-Ln**, it is unknown whether the symmetry observed in **1-Ln**, which results in only three unique Ln–O distances per

complex, is maintained. The mass spectrometry data also support the structural assignments of **1-Ln**, **3-Ln**, and **4-Ln** that were determined by X-ray crystallography.

Structural data for the bidentate $[pin^F]^{2-}$-containing complexes $[Ln(pin^F)_2(THF)_3]^-$, **3-Ln**, and $[Ln(pin^F)_2(THF)_2]^-$, **4-Ln**, are compared in Table 2 and Table S5. An example of the seven coordinate $[K(THF)_2][Ln(pin^F)_2(THF)_3]$, **3-Ce** is shown in Figure 2 and **3-Nd** is in Figure S2. The complexes are similarly monoanionic but possess an inner-sphere K^+ countercation. The K^+ center exhibits long bonds with oxygen atoms of $[pin^F]^{2-}$, O(3) and O(4), as well as the fluorine atoms of $[pin^F]^{2-}$ and the oxygen atoms of THF (Figure 2). These types of interactions, in which fluorine demonstrates an affinity for oxophilic metal centers, are commonly seen in fluorinated lanthanide complexes.[19, 109-110] These interactions in the solid state hold the $[pin^F]^{2-}$ ligands in a rigid, asymmetric fashion, leaving an open site on the opposite side of the metal center where THF ligands can coordinate.

Table 2. Selected distances (Å) and angles (°) in crystal structures of **3-Ln** and **4-Ln**

	3-Ce	**3-Nd**[a]	**4-Eu**	**4-Gd**	**4-Dy**	**4-Y**
Ln(1)–O(3)[b]	2.404(3)	2.369(3)	2.293(4)	2.257(8)	2.260(2)	2.234(2)
Ln(1)–O(4)[b]	2.399(3)	2.370(3)	2.267(4)	2.284(8)	2.231(2)	2.254(2)
Ln(1)–O(5)[c]	2.337(3)	2.314(3)	2.222(4)	2.226(8)	2.184(2)	2.185(2)
Ln(1)–O(6)[c]	2.349(3)	2.309(3)	2.235(4)	2.209(8)	2.190(3)	2.176(2)
Ln(1)–O(7)[d]	2.518(4)	2.495(3)	2.413(4)	2.399(8)	2.380(2)	2.352(2)
Ln(1)–O(8)[d]	2.576(3)	2.516(4)	2.412(4)	2.381(9)	2.385(2)	2.360(2)
Ln(1)–O(9)[d]	2.573(3)	2.536(3)	e	e	e	e
K(1)–O(3)	2.637(3)	2.646(4)	2.653(4)	2.633(8)	2.682(3)	2.646(2)
K(1)–O(4)	2.632(3)	2.629(4)	2.631(4)	2.656(9)	2.625(3)	2.680(2)
O(3)–Ln(1)–O(4)	74.41(11)	74.27(11)	80.18(13)	80.4(3)	80.02(9)	81.06(8)
O(3)–Ln(1)–O(5)	66.45(11)	67.04(12)	69.89(13)	69.8(3)	70.72(9)	71.15(8)
O(4)–Ln(1)–O(6)	66.10(11)	66.92(12)	69.91(13)	69.9(3)	70.34(10)	71.23(7)
Pln1–Pln2[f]	5.73	4.48	19.23	19.07	17.37	18.84

[a]Ln(1) is used to represent atom Nd(2) for **3-Nd**

[b]O(3) and O(4) are oxygen atoms of $[pin^F]^{2-}$ that are proximal to and share an interaction with K^+

[c]O(5) and O(6) are oxygen atoms of $[pin^F]^{2-}$ that are distal to K^+

[d]O(7)-O(9) are oxygen atoms of THF

[e]O(9) of THF is not present for 6-coordinate species **4-Ln**

[f]Pln1 and Pln2 are the Planes of (Ln(1), O(3), O(4)) and (K(1), O(3), O(4)), respectively

The presence of an inner-sphere K^+ ion results in a diamond core at the center of the complex marked by atoms Ln(1), O(3), O(4), K(1). For larger rare earth metals (**3-Ln**, Ln = Ce, Nd) this diamond core is close to planar, but for the smaller rare earths (**4-Ln**, Ln = Eu, Gd, Dy, Y) the core is more bent. In the **4-Ln** series, each Ln atom is six-coordinate with one less THF molecule bound than in the **3-Ln** complexes. Figure 3 shows a slightly more open environment at **4-Eu**, and **4-Gd**, **4-Dy**, and **4-Y** are shown in Figures S3, S4, and S5 respectively. Scheme 3 shows a generic **4-Ln** complex and how the two planes, pln1 and pln2 are defined. The angle between the plane of Ln(1), O(3), O(4) (pln1) and the plane of K(1), O(3), O(4) (pln2) generally increases with a decrease in rare earth radial size resulting in a more bent structure for the smaller metals: 5.73° (**3-Ce**); 4.48° (**3-Nd**); 19.23° (**4-Eu**); 19.07° (**4-Gd**); 17.37° (**4-Dy**). Complex **4-Y** is an outlier in this trend: 18.84° (**4-Y**). On the convex side of the angle between pln1 and pln2, there exist long $K\cdots F$ interactions between the inner-sphere K^+ ion and F atoms of $[pin^F]^{2-}$. Interestingly, for the smaller rare earths (**4-Ln**, Ln = Eu, Gd, Dy, Y) where there is a greater pln1–pln2 angle, there are only three $K\cdots F$ interactions, whereas in the complexes of larger rare earth metals (**3-Ln**, Ln = Ce, Nd) there are four, suggesting that the angle of the bent core is independent of $K\cdots F$ interactions.

plane 1 (pln1) : Ln(1) O(3) O(4)

plane 2 (pln2) : K(1) O(3) O(4)
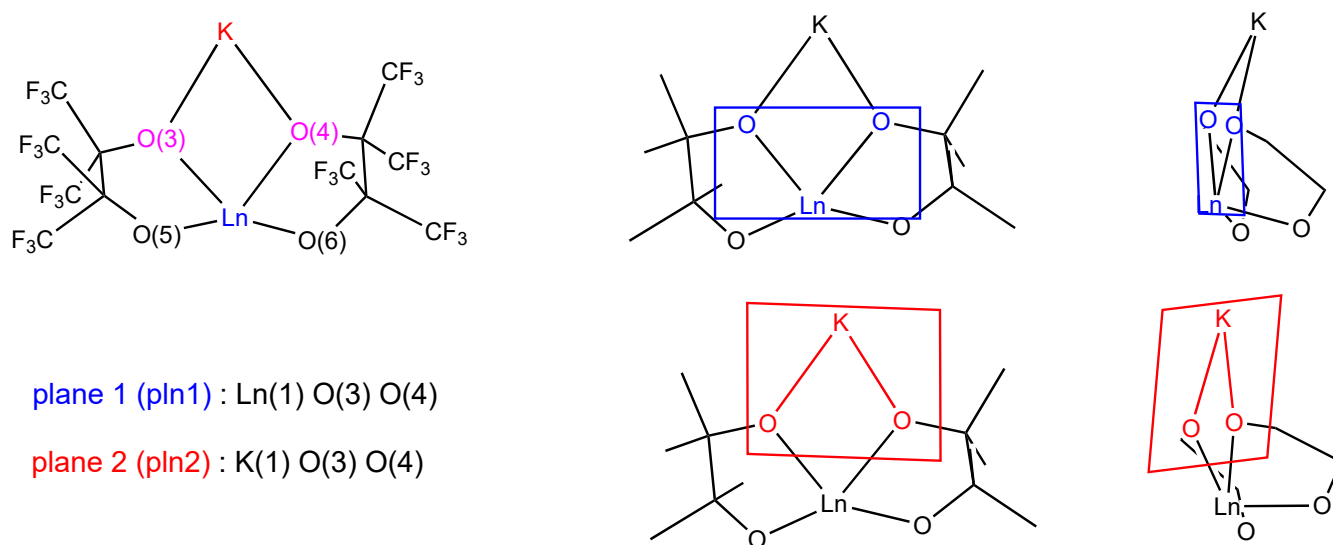
Scheme 3. Definitions of plane 1 and plane 2, used to calculate angles in Table 2. Sketches have been simplified for clarity with sequential loss of (left) THF ligands, (center) fluorine atoms, and (right) methyl groups.

15

The two bond distances between the K^+ and O atoms of $[pin^F]^{2-}$, K(1)–O(3) and K(1)–O(4), are the same for the larger rare earth metals (**3-Ln**, Ln = Ce, Nd). For the smaller rare earths (**4-Ln**, Ln = Eu, Gd, Dy, Y), there is a lack of a consistent trend, where K(1)–O(3) and K(1)–O(4) are the same for the **4-Eu** and **4-Gd**, while an apparent asymmetry exists for **4-Dy** and **4-Y**. An asymmetry in $[pin^F]^{2-}$ coordination resulting from K(1)–O(3) and K(1)–O(4) bonds that is common for all **3-Ln** and **4-Ln** complexes can be seen in how the ligands are bent around the rare earth metal center, toward the K^+ ion. Bond angles O(3)–Ln(1)–O(4) are significantly shorter than the O(5)–Ln(1)–O(6) angles, and generally increase as radial size decreases. For each complex, angles between the rare earth metal and the O atoms of a given $[pin^F]^{2-}$ ligand, O(3)–Ln(1)–O(4) and O(3)–Ln(1)–O(5), are the same as one another.

The bond lengths between the rare earth centers and the oxygen atoms of $[pin^F]^{2-}$ that share an interaction with K^+, Ln(1)–O(3) and Ln(1)–O(4), are generally the same length as one another and shorter than the Ln(1)–O(5) and Ln(1)–O(6) distances to the two THF molecules. Exceptions include in **4-Eu** where Eu(1)–O(3), 2.293(4) Å, is longer than Eu(1)–O(4), 2.267(4) Å, and in **4-Gd** where Gd(1)–O(3), 2.257(8) Å, and Gd(1)–O(5), 2.226(8) Å, are the same within error. For the smaller rare earth metals that are six-coordinate, there is no difference in bond length between the metal centers and the two coordinated THF molecules, Ln(1)–O(7) and Ln(1)–O(8). However, for the larger rare earths that are seven-coordinate, two of the THF molecules are at a further distance than the third. In **3-Ce**, Ce(1)–O(8) and Ce(1)–O(9) are similar with bond distances of 2.576(3) Å and 2.573(3) Å, respectively, while the third, Ce(1)–O(7), is demonstrably shorter at 2.518(4) Å. The same pattern is seen in **3-Nd** where Nd(1)–O(8) and Nd–O(9) (2.516(4) Å and 2.536(3) Å) are longer than Nd(1)–O(7) (2.495(3) Å). The longer Ln(1)–O(7) bond may result from repulsion with the closest CF_3 groups of $[pin^F]^{2-}$, which is less present on the other side of the molecule where K···F interactions are found.

Within $[pin^F]^{2-}$ the O–C bond distances are similar and unexceptional, as is evident in **3-Ce**: O(3)–C16, 1.364(5) Å; O(4)–C10, 1.360(5) Å; O(5)–C19, 1.347(6) Å; O(6)–C13, 1.350(5) Å. The C10–C13 and C16–C19 distances of the $[pin^F]^{2-}$ backbone are similar, 1.658(7) Å and 1.668(7) Å, respectively, but are significantly longer than that of a typical Csp^3–Csp^3 bond of 1.54 Å.[111] Such elongated bonds are characteristic of the pin^F dianion when chelating a metal center.[26] The C–F distances within $[pin^F]^{2-}$ vary from 1.326(7) Å (C18–F19) to 1.355(6) Å (C17–C10), but are all the same within error, indicating that the interactions between K^+ and the F atom of $[pin^F]^{2-}$ do not result in a change in C–F bond lengths.

Concomitant with the decrease in coordination number is a change in Ln–O(pin^F) bond lengths.[112-113] Subtracting the ionic radius[114] of each Ln^{III} ion from its average Ln–O(pin^F) length normalizes the

distances from the metal center to the ligand in a method inverse to that of using a constant ionic radius of O^{2-} (oxide) to study the ionic radii of the lanthanides.[115-116] The results of this analysis are presented in Table 3 and show that there is a distinct difference between the six- (**4-Ln**) and seven- (**3-Ln**) coordinate complexes, beyond the change in coordination number: the average Ln–O(pin^F) distances are longer for the smaller ions, despite the steric relief provided by removal of one THF ligand. The difference in Ln–O(pin^F) distances **4-Ln** and **3-Ln** is reduced when the Ln–O(THF) distances are included in the averages (Table S3), indicating that it is primarily the $[pin^F]^{2-}$ ligands that experience increased strain. This difference is consistent with the rigidity of the molecular structure, as the bidentate nature of $[pin^F]^{2-}$, coupled with the steric bulk of four CF_3 groups and the interaction of K^+, restricts the ligands flexibility in the tight coordination environment.

Table 3. Normalization of Ln(1)–O(O(3)-O(6)) distances (Å) in $[pin^F]^{2-}$ complexes.

	3-Ce	**3-Nd**	**4-Eu**	**4-Gd**	**4-Dy**	**4-Y**
Coordination Number	7	7	6	6	6	6
Ln^{III} Ionic Radius[117]	1.07	a	0.947	0.938	0.912	0.9
Avg. Ln–O Distance^b	2.372	2.341	2.255	2.244	2.216	2.212
Normalized Ln–O Distance	1.302		1.308	1.306	1.304	1.312

^{a}not available for 7-coordinate Nd^{3+}

^{b}average bond distance of Ln(1)–O(O(3)-O(6))

There are few other crystallographically characterized examples of mononuclear Ce^{III} complexes in which all seven coordinating atoms are oxygen donors. Only five entries in the CSD[12] ([Li_3(THF)_4][(BINOLate)_3Ce(THF)][118], [Li(THF)_2][Li(THF)][Li(OPPh_3)][(BINOLate)_3Ce(OPPh_3)][66], [Li(DME)_3][(BINOLate)_3Ce(OPPh_3)][66], Ce(Ph_2P(O)NP(O)Ph_2)_3(THF)[119], [Ce(OTf)_2(OPPh_3)_4][OTf][120]) meet these criteria. Ce–O distances range from 2.337 Å to 2.650 Å,[120] with a mean of 2.44 Å (Table S2).[65-66, 118-120] Thus, **1-Ce** and **3-Ce** are new contributions to a very small family of complexes. Mononuclear six- and seven-coordinate Nd complexes in all-oxygen donor environments are also rare, with only six[67, 114, 121-124] and eight[25, 125-131] entries in the CSD, respectively.

All these fluorinated alkoxide compounds are new members of a rather small family of compounds. There are approximately 2800 structures of non-polymeric lanthanide complexes containing fluorine anywhere in their crystal structures,[12] of which about 500 have only triflate as a fluorine source. The majority feature fluorinated β-diketonates, such as hexafluoroacetylacetonate (hfac), as ligands ancillary to non-fluorinated ligands under principal study. There are only 65 unique species that have neither a β-

diketonate nor a triflate ligand (details of this survey are shown in Scheme S1). One other crystallographically characterized monometallic Ln species[132] contains two pin^F-derived ligands, but unlike **3-Ce**, it has two phenanthroline co-ligands, namely [Ce^{III}(pin^F)(Hpin^F)(phen)$_2$] (Scheme S2). Its luminescence behavior is also markedly different (*vide infra*), with an absorption wavelength of 310 nm and primary emission at 380 nm. The rigid phenanthroline moieties are partly responsible for the smaller Stokes shift, as very little vibrational energy is lost through C–H bonds.

Having established the structures of these compounds, it was naturally of interest to compare the absorption and emission spectra of **1-Ln** and **2-Ln** to those of **3-Ln** and **4-Ln**. Calculated spectra were then compared to those obtained experimentally to understand the electronic structure of these complexes and to determine the level of contemporary theory appropriate to treat such complexes.

Spectroscopy.

Normalized solution-state absorption and emission spectra of Ce complexes **1-Ce** and **3-Ce** are shown in Figure 4. Both absorb in the UV range and emit in the blue, with the [OC$_4$F$_9$]$^{1-}$-ligated species **1-Ce** displaying higher energy transitions and a smaller Stokes shift. Although the molecular structure of **1-Ce** is less rigid than **3-Ce**, it is hypothesized that the presence of fewer THF ligands results in fewer C–H bonds through which to lose excitation energy via vibrations.

The solid-state excitation and emission spectra of the Ce^{III} complexes are shown in Figure 5. The broad emission bands, attributed to $d \rightarrow f$ transitions,[133-134] are located in the blue region with maxima at ~357 and ~405 nm for the complexes **1-Ce** and **3-Ce**, respectively. The different coordination environments around the Ce^{III} are reflected in the shift, of ~50 nm, between the maxima of the emission bands. Short luminescence lifetimes in the nanosecond range (Table 4, Figures S6 and S7) for the Ce complexes are characteristic of Laporte-allowed d-f transitions.[135]

Table 4: Luminescence lifetimes of Ce and Eu complexes.

	Ce	Eu
Ligand		
[pin^F]$^{2-}$	30.6 ± 0.1 ns	0.935 ± 0.001 ms
[OC$_4$F$_9$]$^{2-}$	5.0 ± 0.1 ns	1.230 ± 0.045 ms

Compared to the literature (Table S4), the solid-state emission of **1-Ce** is the third most blue-shifted of 49 monometallic Ce species that were reported along with their luminescence properties. Only cerium triflate in THF[135] and hexachlorocerate in acetonitrile[136] show emissions at lower wavelengths. A full comparison is available in Table S4. In the solution phase, however, the luminescence of **1-Ce** and **3-Ce** are within a more commonly observed range.

The solid-state excitation and emission spectra of the Nd^{III} complexes **1-Nd** and **3-Nd** are shown in Figure 6. The excitation spectra of the complexes are composed of characteristic Nd^{III} $f\text{-}f$ intraconfigurational transitions. All the expected $^4F_{3/2} \rightarrow {}^4I_J$ ($J = 9/2$, 11/2 and 13/2) transitions are observed, and the $^4F_{3/2} \rightarrow {}^4I_{11/2}$ transition is the most intense one. Compared to the spectra of **1-Ce** and **3-Ce** above, those of **1-Nd** and **3-Nd** do not change appreciably with the substitution of the ligands, which is consistent with expected lanthanide emission behavior and further highlights the difference seen in the cerium complexes.

The solid-state excitation and emission spectra of the Eu^{III} complexes **2-Eu** and **4-Eu** are shown in Figure 7, and the emission decay curves are in Figures S8 and S9, respectively. As for all the lanthanides studied here, except Ce, the excitation spectra are dominated by the f-f transitions, indicating that the emission occurs through direct metal-centered excitation, instead of ligand-mediated sensitization. The Eu-containing complexes have a longer lifetime than Ce, in the millisecond range, characteristic of forbidden nature of the $f\text{-}f$ transitions (Table 4). All the expected characteristic narrow $^5D_0 \rightarrow {}^7F_J$ ($J = 0 - 4$) transitions are observed, and the $^5D_0 \rightarrow {}^7F_2$ transition is the most intense one. In the emission spectra the differences in fine splitting seen for each $^5D_0 \rightarrow {}^7F_J$ ($J = 0 - 4$) transition of each complex highlight the change in symmetry around the Eu^{III} ions in both complexes. For example, the $^5D_0 \rightarrow {}^7F_0$ transition is present and fairly intense for **4-Eu**, while mostly absent for **2-Eu**. The symmetry around Eu in **4-Eu** [K(THF)$_2$][Eu(pin^F)$_2$(THF)$_3$] ($\sim C_{2v}$) is lower than that in the presumed structure of **2-Eu**, [K(THF)$_6$][Eu(OC$_4$F$_9$)$_2$(THF)$_2$] ($\sim O_h$),[137, 140] consistent with the difference in intensity for 0-0 peak. The $^5D_0 \rightarrow {}^7F_1$ transition of the two compounds also differ, with more fine structure for **4-Eu**. This behavior is further mirrored in the $^5D_0 \rightarrow {}^7F_2$ transition, which has a completely different profile for both complexes, with more intense fine structure components for the complex with lower symmetry, as expected. The differences in symmetry are reflected as well in the calculated excitation spectra (Figures 13 and 14). While the experimental spectra are not sharp enough at room temperature to enable extensive symmetry discussions, the calculated spectra are distinctively different as discussed below.

The excitation and emission spectra of the Dy^{III} complexes **2-Dy** and **4-Dy** are shown in Figure 8. The excitation spectra are composed of only characteristic Dy^{III} $f\text{-}f$ intraconfigurational transitions ($^4H_{13/2} \leftarrow$ $^6H_{15/2}$ ~298 nm, ($^6P_{3/2} + {}^4K_{15/2}$) $\leftarrow {}^6H_{15/2}$ ~324 nm, ($^4M_{15/2} + {}^6P_{7/2}$) $\leftarrow {}^6H_{15/2}$ ~350 nm, ($^6P_{5/2, 3/2}$) $\leftarrow {}^6H_{15/2}$

~364 nm, ($^4M_{21/2, 19/2}$ + $^4K_{17/2}$ + $^4F_{7/2}$ + $^4I_{13/2}$) ← $^6H_{15/2}$ ~378 – 404 nm, $^4G_{11/2}$ ← $^6H_{15/2}$ ~423 nm).[138] The $^4F_{9/2}$ → $^6H_{13/2}$ transition is the most intense.

All the d^0 Y- and f^7 Gd-containing complexes (**4-Y**, **2-Gd**, and **4-Gd**, respectively) are expected to be non-emissive under illumination and were not studied in their pure form. Lifetime measurements of **2-Dy** and **4-Dy** were complicated due to apparent concentration quenching of the excited state.[139-141] The synthesized Gd^{III} complexes were mixed with their corresponding Dy^{III} analogs, in an effort to dilute the Dy^{III} centers in the solid state and minimize the quenching, but the attempts were not successful. Five mixed Gd/Dy samples each for **2-Gd/Dy** and **4-Gd/Dy** (% Gd = 90, 75, 50, 25, 10; balance Dy) were prepared and attempts were made to record their luminescence lifetimes, but apparent quenching persisted. Attempts were also made with 0.1% and 0.05% Dy in predominantly Gd samples, but no differences were observed versus the pure Dy samples.

Due to the absence of sensitized emission, further in depth photophysical characterization of the complexes was not pursued. We focussed instead on modelling the spectroscopic behaviour in the solid state.

Computational.

Geometry-optimized gas-phase structures of compounds **1-Ce** and **3-Ce** show Ce–O distances all within 0.1 Å of the corresponding values in the crystal structures (Table S5). The symmetry observed in **1-Ce** is preserved in the gas phase, with three distinct Ce–O distances rather than six. The same level of accuracy was obtained for **1-Nd** and **3-Nd**, but in the case of **1-Nd**, the symmetry was lost upon optimization. The average Ln–O(pin^F) distances for **3-Nd**, **4-Eu**, **4-Dy**, and **4-Y** were all within 0.04 Å of the calculated distances. Gas-phase geometries were not able to be obtained for **2-Gd** or **4-Gd**.

Ln–O bonds in the gas-phase optimized structures of **1-Ln**, **2-Ln,** **3-Ln**, **4-Ln**, and **4-Y** were evaluated using both canonical orbital and NBO analyses and two measures of bond order: Mayer (MBO) and Wiberg (WBO). The WBOs are small for Ln–THF bonds, below 0.14 for all complexes studied, and MBOs are similarly reduced relative to Ln–O(pin^F) bond orders. The Ln–O(C_4F_9) bonds have higher bond orders, consistent with the difference in bond lengths seen in Table 2. There is asymmetry in the [pin^F]$^{2-}$ ligand environments of **3-Ce**, **3-Nd**, **4-Eu**, **4-Dy**, and **4-Y**, with the bond order of Ln(1)–O(3) and Ln(1)–O(4) being slightly but consistently lower than the others (Table 5). This difference in bond order is

accompanied by longer bond lengths. The K(1)···O(3) and K(1)···O(4) bonds are ionic and very little sharing of electron density is observed in the calculations.

It can also be seen in Table 5 that the Y–O(pin^F) bonds are similar to the other Ln–O(pin^F) bonds. It is commonly observed that Y^{III} is able have stronger orbital bonds with hard ligands, but in this case the WBO suggests that the [pin^F]$^{2-}$ ligands interact predominately through electrostatic means. This idea is supported by the natural electron configuration of the yttrium center that contains only 0.82 non-core d-electrons. This result is similar to the occupation of the d-orbitals in the **3-Ln** and **4-Ln** complexes, which range between 0.66 for **3-Ce** to 0.80 for **4-Dy**.

Table 5: Comparisons of Ln–O distances and bond orders in gas-phase optimized structures of $[\text{pin}^\text{F}]^{2-}$ species **3-Ln** and **4-Ln**.

	Bond	Distance (Å)	MBO	WBO
3-Ce	Ce(1)–O(3)	2.373	0.50	0.21
	Ce(1)–O(4)	2.372	0.50	0.21
	Ce(1)–O(5)	2.356	0.59	0.23
	Ce(1)–O(6)	2.357	0.59	0.23
3-Nd[a]	Nd(1)–O(3)	2.371	0.47	0.20
	Nd(1)–O(4)	2.366	0.49	0.20
	Nd(1)–O(5)	2.321	0.58	0.22
	Nd(1)–O(6)	2.309	0.63	0.23
4-Eu	Eu(1)–O(3)	2.327	0.55	0.24
	Eu(1)–O(4)	2.329	0.54	0.23
	Eu(1)–O(5)	2.256	0.68	0.28
	Eu(1)–O(6)	2.255	0.67	0.27
4-Dy	Dy(1)–O(3)	2.241	0.54	0.23
	Dy(1)–O(4)	2.246	0.54	0.23
	Dy(1)–O(5)	2.176	0.70	0.28
	Dy(1)–O(6)	2.182	0.69	0.28
4-Y	Y(1)–O(3)	2.262	0.68	0.24
	Y(1)–O(4)	2.257	0.69	0.25
	Y(1)–O(5)	2.190	0.82	0.28
	Y(1)–O(6)	2.190	0.82	0.28

[a]Nd(1) is used to represent atom Nd(2) for **3-Nd**

An overlay of the solution-state, solid-state, and simulated gas-phase absorption spectra for Ce-containing **1-Ce** is presented in Figure 9. Whereas vibronic coupling is observed in the solution-phase data, the same features are not found in either the solid state or calculated spectra. In the gas phase, three main transitions comprise the single broad peak, and the MOs contributing the most to each excited state are visualized in Figure 10. Each of the excited states is best characterized as an excitation from the Ce $4f$ SOMO to a $5d$ orbital (Table 6). Good agreement with experiment was found for the calculated absorption spectrum of **3-Ce** (Figure 11) and the calculated absorptions transitions with the main contributing MOs for **3-Ce** (Figure 12).

Table 6. Atomic orbital contributions to excited states in **1-Ce** and **3-Ce**, determined from the compositions and CI expansion coefficients of the dominant positive transitions in each case.

	Excited State	Acceptor MO	CI Coefficient	% Ce d in MO	% Ce f in MO
1-Ce	7	290 A	0.92747	72.99	-
	8	291 A	0.96241	70.07	-
	9	292 A	0.94035	73.52	-
3-Ce	7	292 A	0.43868	40.88	-
		296 A	0.40906	56.63	12.11
		297 A	0.51404	27.97	-
	8	298 A	0.90483	63.75	-

The absorption spectra of the Nd^{III} complexes **1-Nd** and **3-Nd** were modeled using QDPT+NEVPT2/SA-CASSCF and QDPT-SORCI^{emb}/SA-CASSCF^{emb} calculations (herein referred to as NEVPT2 and SORCI^{emb}). The results are shown in Figures S10, S11, S12 and S13, with the energy levels and peak assignments shown in Table S6-S7. It can be seen that both the NEVPT2 and SORCI^{emb} calculations adequately reproduce the relative positions of the spectral features for both **1-Nd** and **3-Nd**, while the absolute positions of the excitations are blue-shifted by approximately 40 nm (2778 cm^{-1}).

As was hinted at above, there is very little difference between the excitation spectra of **1-Nd** and **3-Nd**. Nonetheless, we did attempt to validate our theoretical models by assessing their ability to reproduce slight discrepancies in peak positions/intensities/splitting. If the theoretical models are unable to reproduce these discrepancies, then their utility in validating structural assignments based on spectroscopic data is less powerful. We first note that the fine structure of the $^4G_{5/2} + {}^4G_{7/2} \leftarrow {}^4I_{9/2}$ peaks at ~590 nm is completely lost when using the QDPT-SORCI^{emb}/SA-CASSCF^{emb} model. This result immediately suggests that this fine structure is a result of orbital interactions between the metal center and the ligands. As will be shown below, the other Eu and Dy species that were modeled did not display fine structure that was not captured by the SORCI^{emb} model. This difference may be due the greater number of empty f-orbitals in the Nd^{III} species that are able to act as acceptors for the ligands.

There are two other main discrepancies between the excitation spectra of **1-Nd** and **3-Nd**. The first is the intensity of the $^4G_{11/2} + {}^2K_{15/2} + {}^2D_{3/2} \leftarrow {}^4I_{9/2}$ peaks at centered at ~470 nm. It can be seen that the peak at the high energy end of this group of peaks is more intense for **3-Nd** and both the NEVPT2 and SORCI^{emb} calculations reflect this feature. The second discrepancy is the splitting of the group of the peak(s) at ~355

nm. This peak is split in the spectrum for **3-Nd** but appears as a single peak for **1-Nd**. The NEVPT2 calculation is able to reproduce this feature, but not the SORCI^{emb} model.

Moving to the Eu^{III}-containing species, the SORCI^{emb} calculations greatly outperform the NEVPT2 calculations as can be seen in Figures S14, S15, S16 and S17. In particular, the NEVPT2 model overstabilizes the ^4L_J peaks relative to the other peaks present in the spectra. That being said, the SORCI^{emb} model was not entirely successful, and the high density of both relativistic and non-relativistic states made robust peak assignments unattainable. It is believed that the use of full intermediate couplings would help to overcome some of the shortcomings observed in the models we employed, but currently this calculation is not feasible as this would involve 7 septet roots, 140 quintet roots, 588 triplet roots, and 490 singlet roots.

There are two main visual differences between the excitation spectra of **2-Eu** and **4-Eu**. The first is the peak at ~450 nm in the spectrum of **2-Eu** (Figure 13) that is not present in the excitation spectrum of **4-Eu** (Figure 14) and was not reproduced by either the NEVPT2 or SORCI^{emb} models. The second discrepancy is the intensity of the hypersensitive $^5D_2 \leftarrow {}^7F_0$ peak at ~465 nm. The SORCI^{emb} model was able to reproduce the enhanced intensity of this peak in the excitation spectrum of **4-Eu**.

Both the SORCI^{emb} and NEVPT2 models were more successful in the prediction of the absorption spectra for the Dy^{III} complexes **2-Dy** (Figure S18) and **4-Dy** (Figure S19) as compared with their performance for **2-Eu** and **4-Eu**, with the SORCI^{emb} model once again outperforming the NEVPT2 calculations (Figures S20 and S21). The SORCI^{emb} model was able to reproduce the enhanced intensity of the $^4G_{11/2}$ $\leftarrow {}^6H_{15/2}$ (~425 nm) relative to the $^4F_{9/2} + {}^4I_{15/2} \leftarrow {}^6H_{15/2}$ (~450 nm) observed in **4-Eu**. In addition, the SORCI^{emb} and NEVPT2 models both reduced the intensity of the peak at ~325 nm relative to the peaks centered at ~387 nm when moving from **2-Dy** and **4-Dy**.

SUMMARY

The eleven new species reported herein, grouped by ligand and coordination number, ([K(THF)$_6$][Ln(OC$_4$F$_9$)$_4$(THF)$_2$], **1-Ln** (Ln = Ce, Nd), [K][Ln(OC$_4$F$_9$)$_4$], **2-Ln** (Ln = Eu, Gd, Dy), [K(THF)$_2$][Ln(pin^F)$_2$(THF)$_3$], **3-Ln** (Ln = Ce, Nd), and [K(THF)$_2$][Ln(pin^F)$_2$(THF)$_2$] **4-Ln** (Ln = Eu, Gd, Dy, Y), and are members of the quite small family of mononuclear lanthanide complexes bearing fluorinated alkoxide donors. The fluorescence properties of the cerium complexes **1-Ce** and **3-Ce** depend upon the *d*-orbital splitting effected by these ligands, and further tuning of those ligands (different substituents on pinacolate or the tertiary alkoxide, fluorinated ligands with greater denticity) may

potentially lead to highly blue-shifted luminescence. Lifetime data indicated that **2-Eu** and **4-Eu** emissions are phosphorescent. The emission spectra of the six Nd, Eu, and Dy complexes do not show large differences based on ligand and are generally consistent with the well-known free-ion spectra. Time-dependent DFT results show that **1-Ce** and **3-Ce** undergo allowed $5f{\rightarrow}4d$ excitations, consistent with luminescence lifetime measurements in the nanosecond range. The ability of a pair of multi-reference models to predict the excitation spectra was evaluated. It was found that for the Nd species, the NEVPT2 model that includes the ligand orbitals was able to reproduce some fine structure that was absent in the SORCI^{emb} model. For the Eu and Dy species, however, the SORCI^{emb} model outperformed the NEVPT2 model, suggesting that the lack of orbital interactions in this model is more than made up for by the more robust treatment of correlation provided by SORCI.

SUPPORTING INFORMATION

The supporting information is available free of charge at ..

AUTHOR INFORMATION

Corresponding Author *E-mail: doerrer@bu.edu

ORCID

Linda H. Doerrer: 0000-0002-2437-6374

Jorge H. S. K. Monteiro: 0000-0002-9622-3537

Ana de Bettencourt-Dias: 0000-0001-5162-2393

Christopher M. Kotyk: 0000-0003-4743-0019

Notes

The authors declare no competing financial interests.
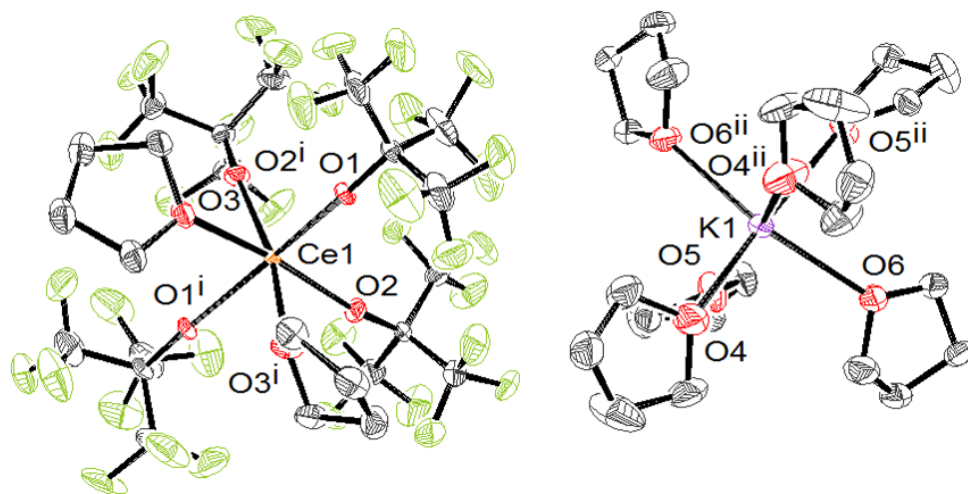
Figure 1. ORTEP of $[K(THF)_6][Ce(OC_4F_9)_4(THF)_2]$ (**1-Ce**). Ellipsoids are drawn at the 50% level. Hydrogen atoms have been removed for clarity.
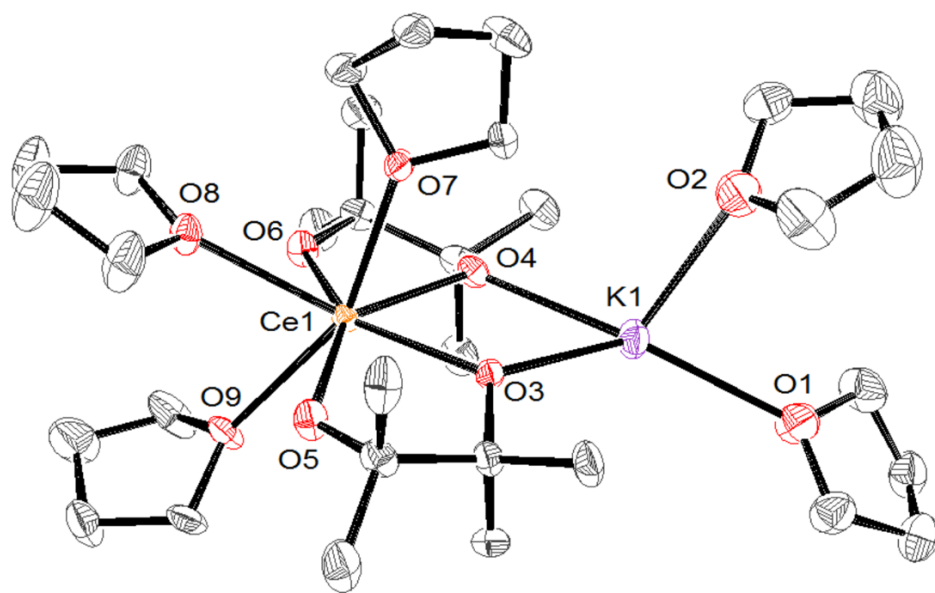
Figure 2. ORTEP of $[K(THF)_2][Ce(pin^F)_2(THF)_3]$ (**3-Ce**). Ellipsoids are drawn at the 50% level. Hydrogen and fluorine atoms have been removed for clarity.
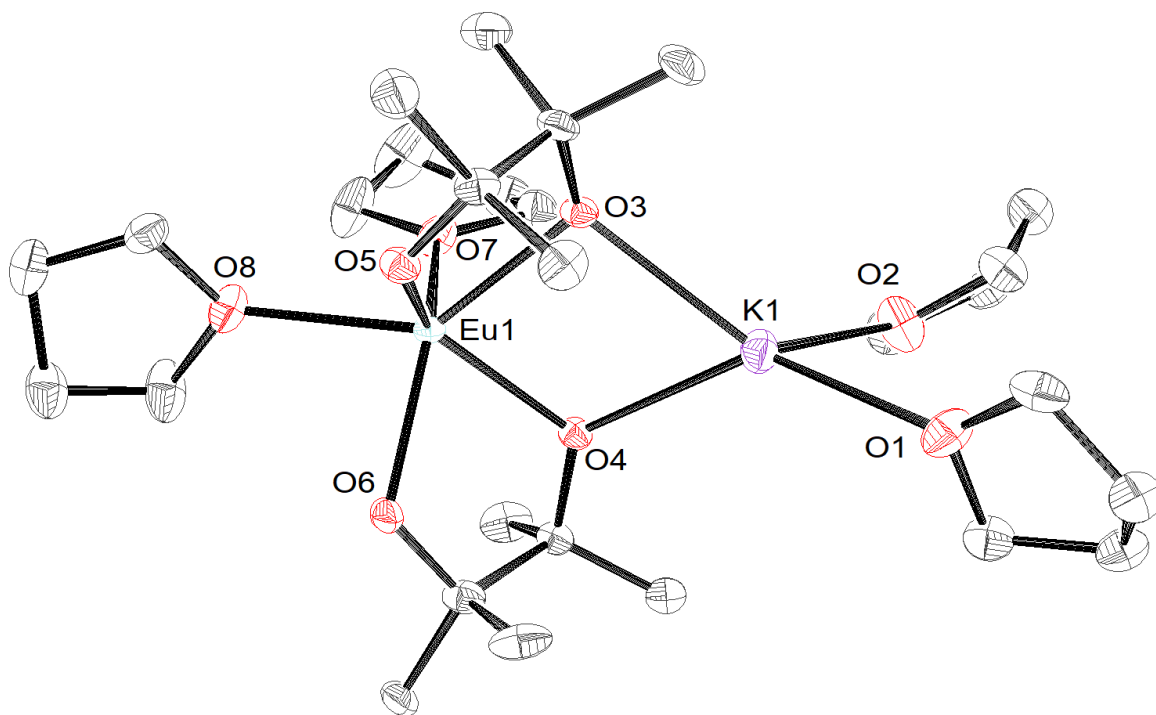
Figure 3. ORTEP of [K(THF)$_2$][Eu(pin^F)$_2$(THF)$_2$] (**4-Eu**). Ellipsoids are drawn at the 50% level. Hydrogen and fluorine atoms have been removed for clarity.
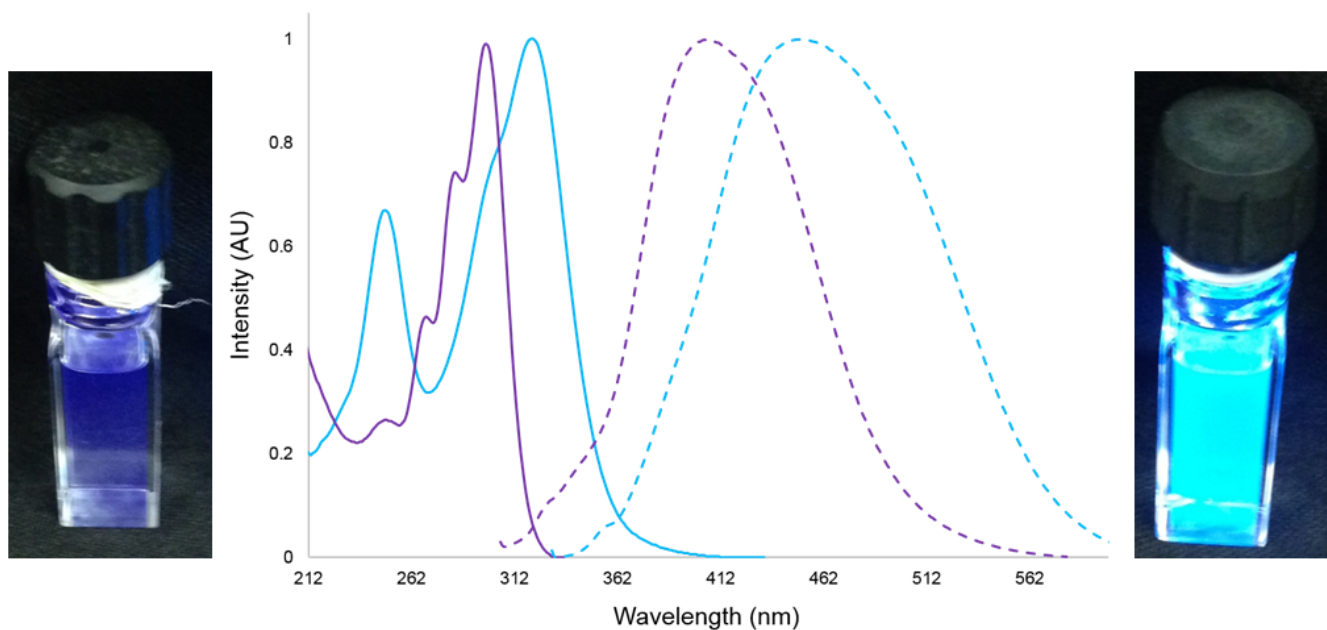
Figure 4. Normalized solution-state excitation and emission spectra of **1-Ce** (purple) and **3-Ce** (blue). Absorption maxima: 298 nm (**1-Ce**); 248, 322 nm (**3-Ce**). Emission maxima: 406 nm (**1-Ce**); 452 nm (**3-Ce**). Photographs of ~0.15 mM **1-Ce** (left) and **3-Ce** (right) in THF were taken under irradiation by 254 nm light.
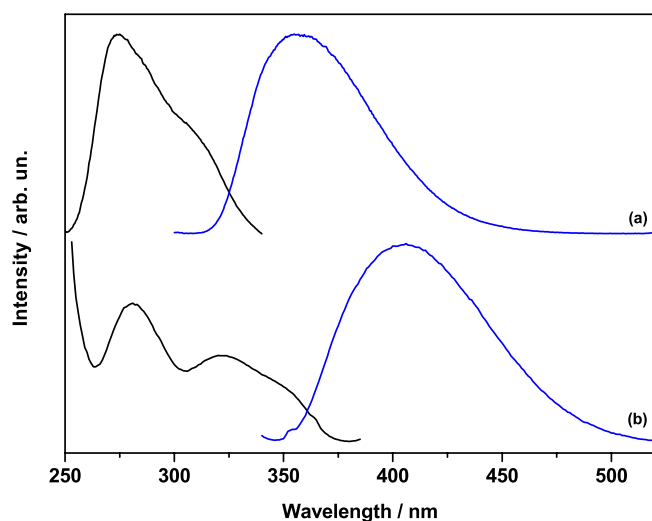
Figure 5. Solid-state excitation and emission spectra of **1-Ce** (top) and **3-Ce** (bottom). Excitation maxima (black traces): 275 nm (**1-Ce**); 281 nm (**3-Ce**). Emission maxima (blue traces): 357 nm (**1-Ce**); 405 nm (**3-Ce**).
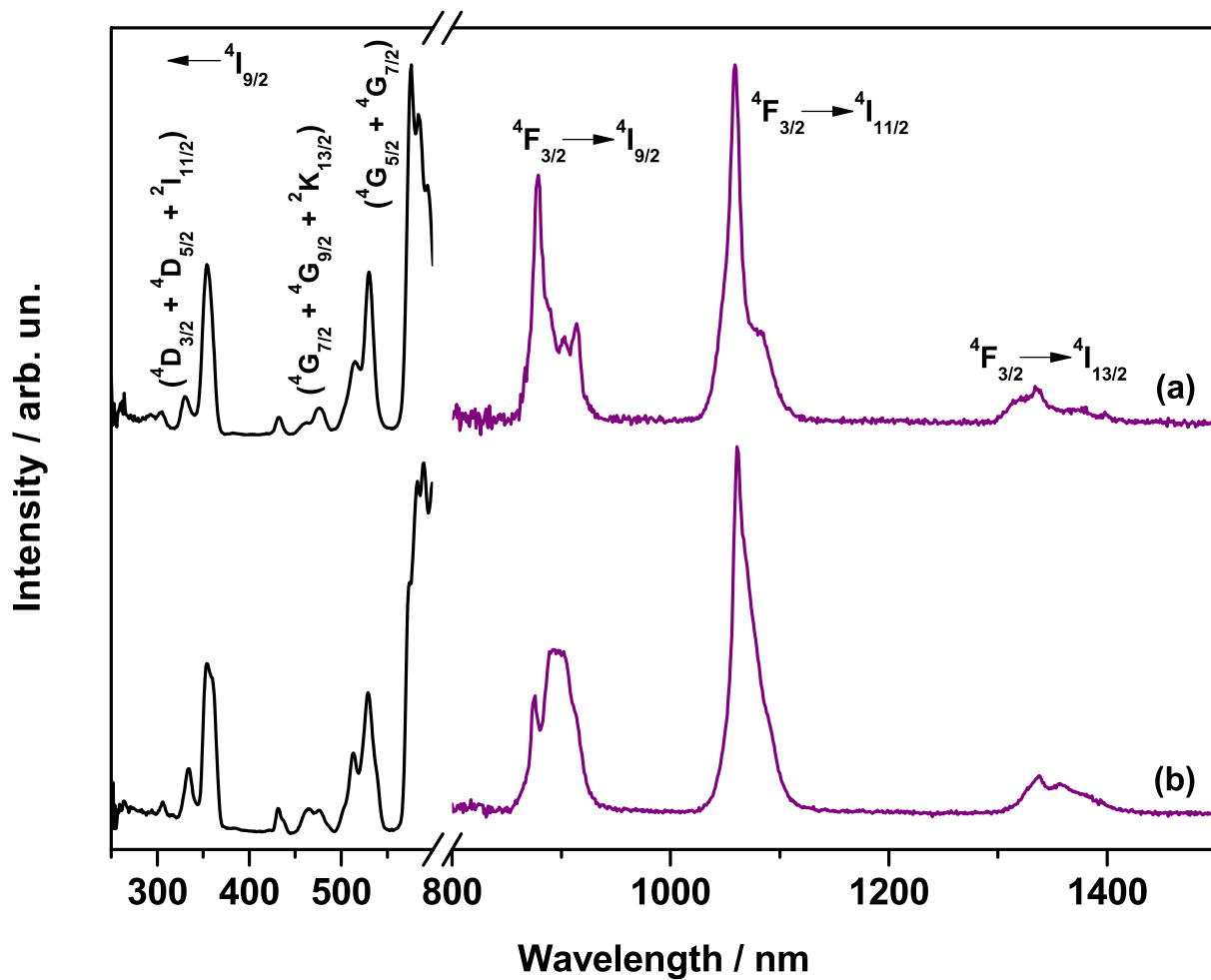
Figure 6. Solid-state excitation and emission spectra of **1-Nd** (a) and **3-Nd** (b) (λ_{exc} = 350 nm).
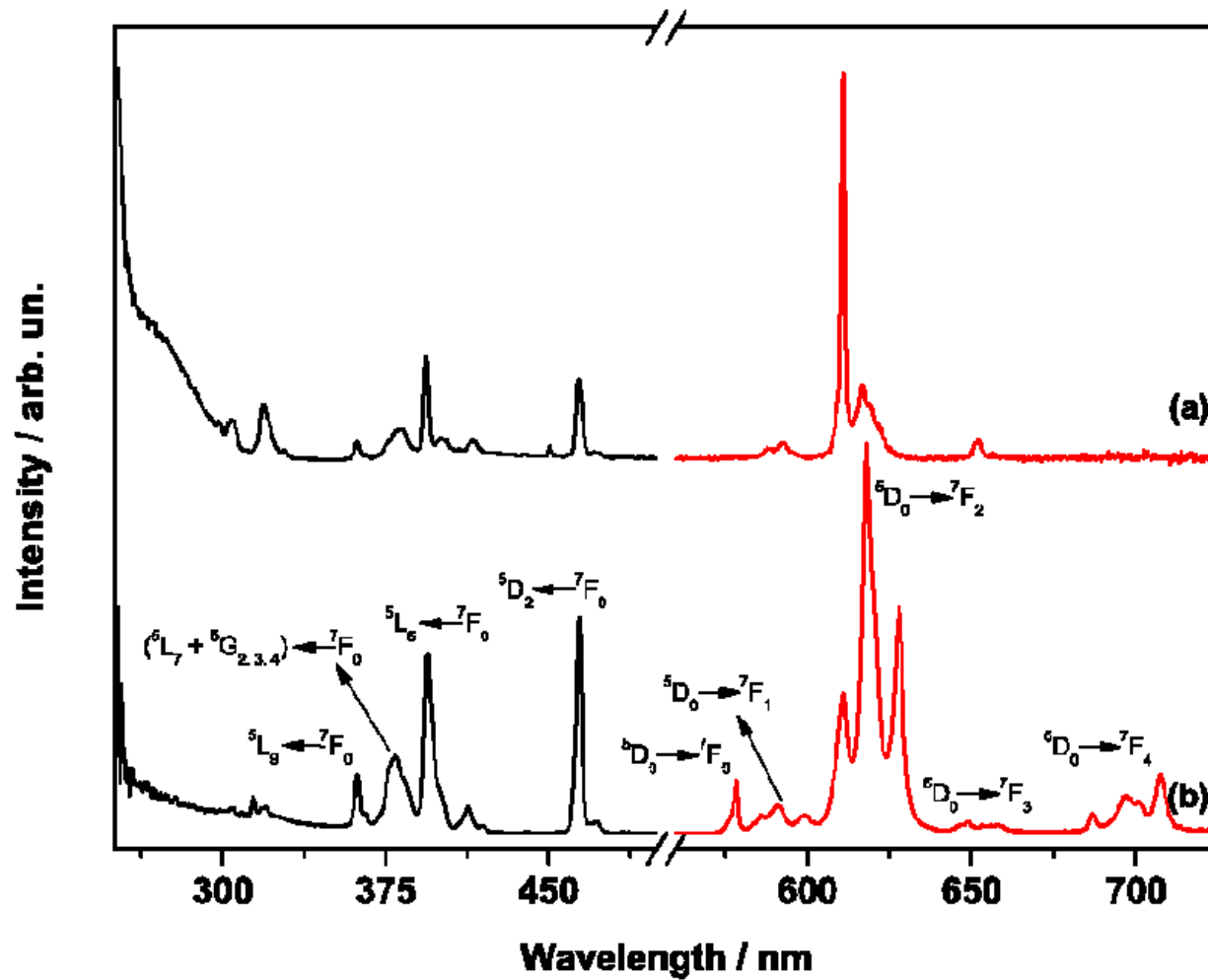
Figure 7. Solid-state excitation and emission spectra of **2-Eu** (a) and **4-Eu** (b) (λ_{exc} = 464 nm).
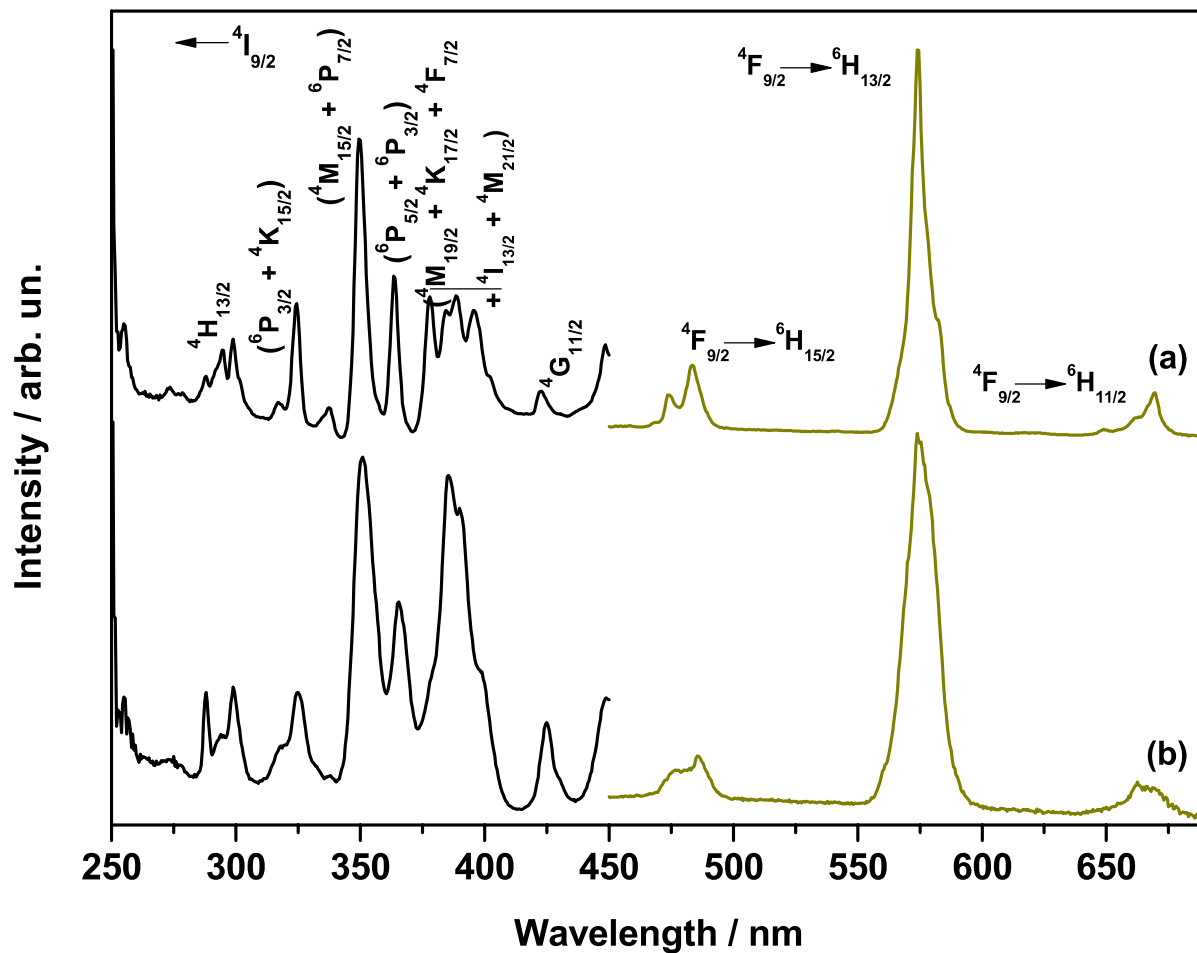
Figure 8. Solid-state excitation and emission spectra of **2-Dy** (a) and **4-Dy** (b) (λ_{exc} = 350 nm).
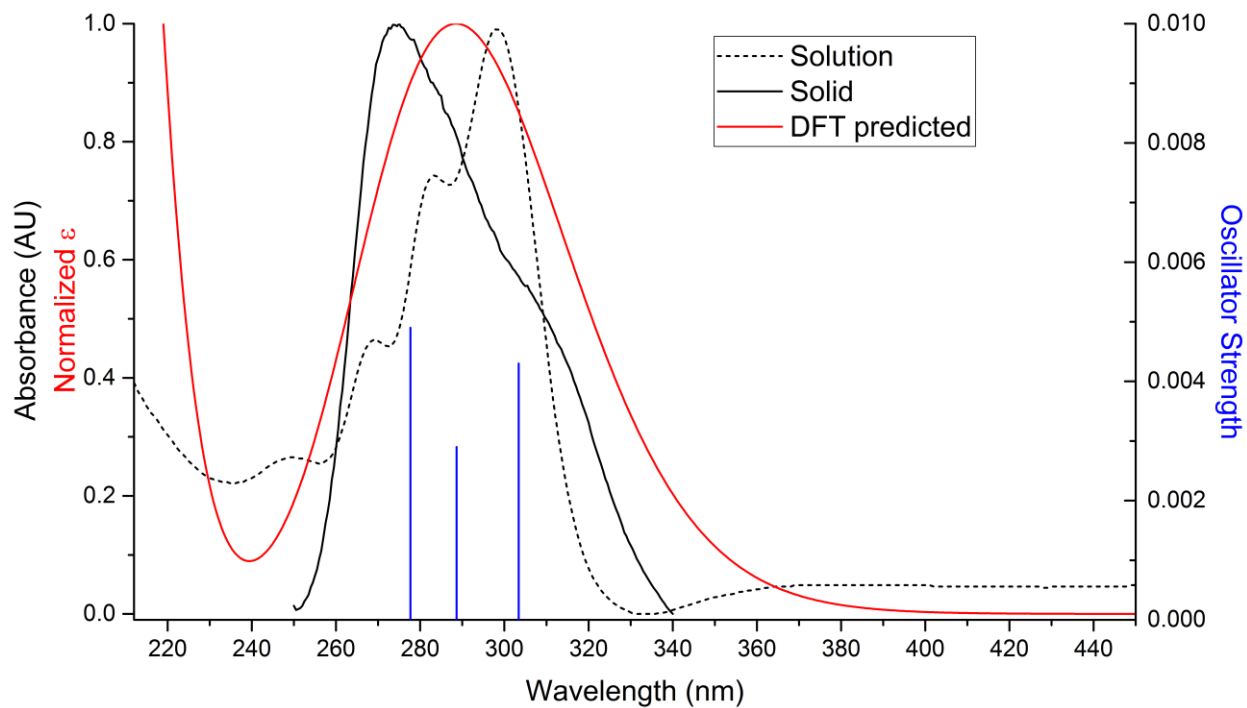
Figure 9. Overlay of solution, solid, and simulated absorption spectra for **1-Ce**. Calculated absorption at 289 nm.
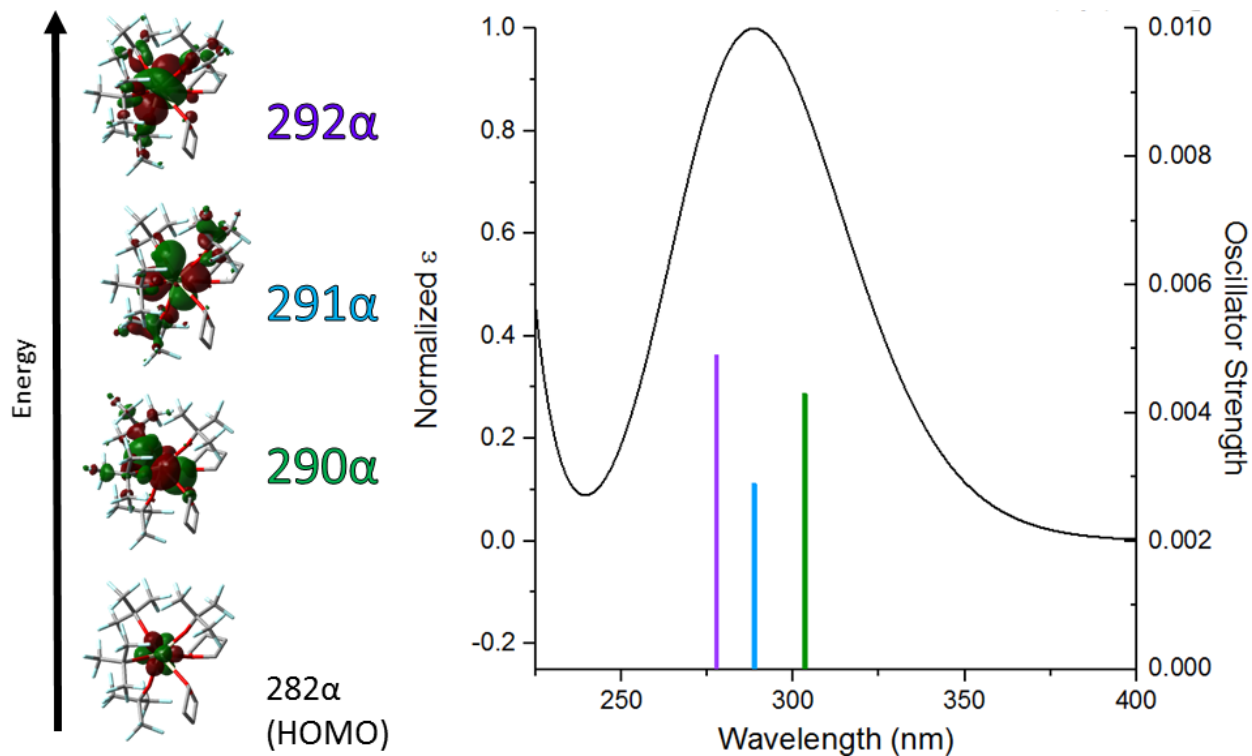
Figure 10. Absorption transitions for **1-Ce** and corresponding donor/acceptor orbitals.
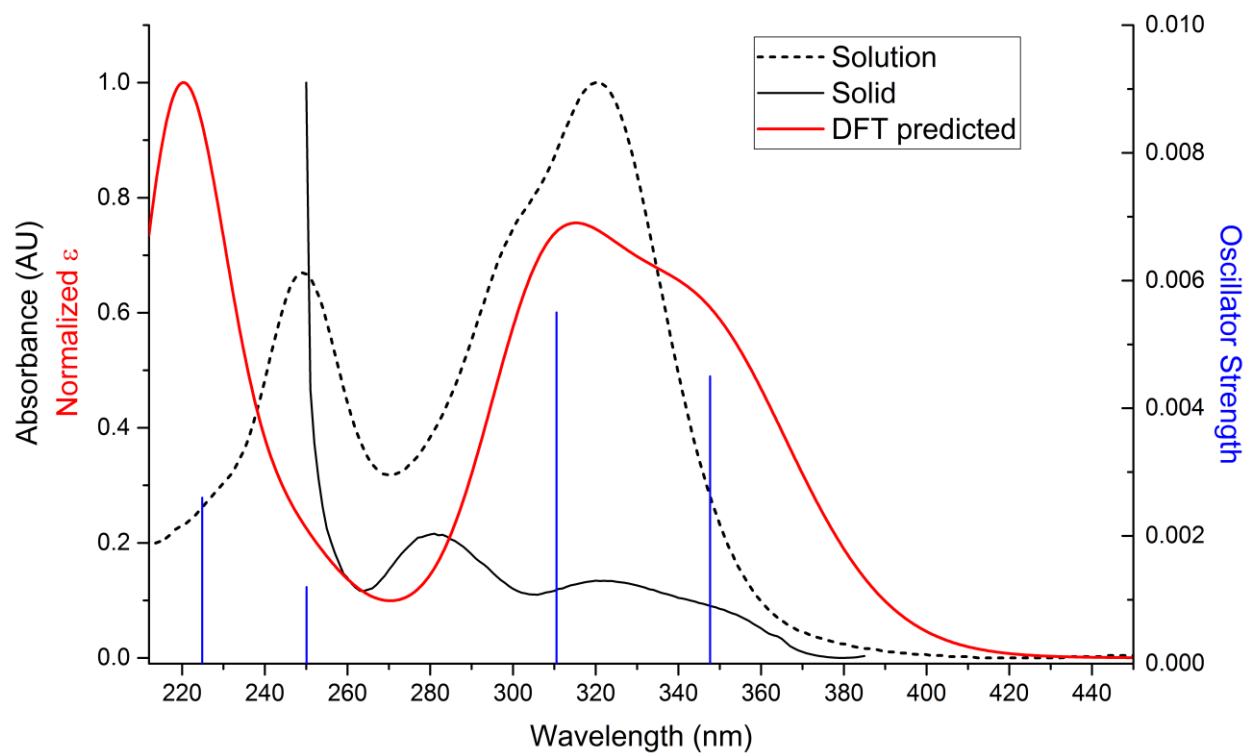
Figure 11. Overlay of solution, solid, and simulated absorption spectra for **3-Ce**. Absorption maxima: 250 and 320 nm (solution); 281 and 320 nm (solid); 221 and 315 nm (calculated).
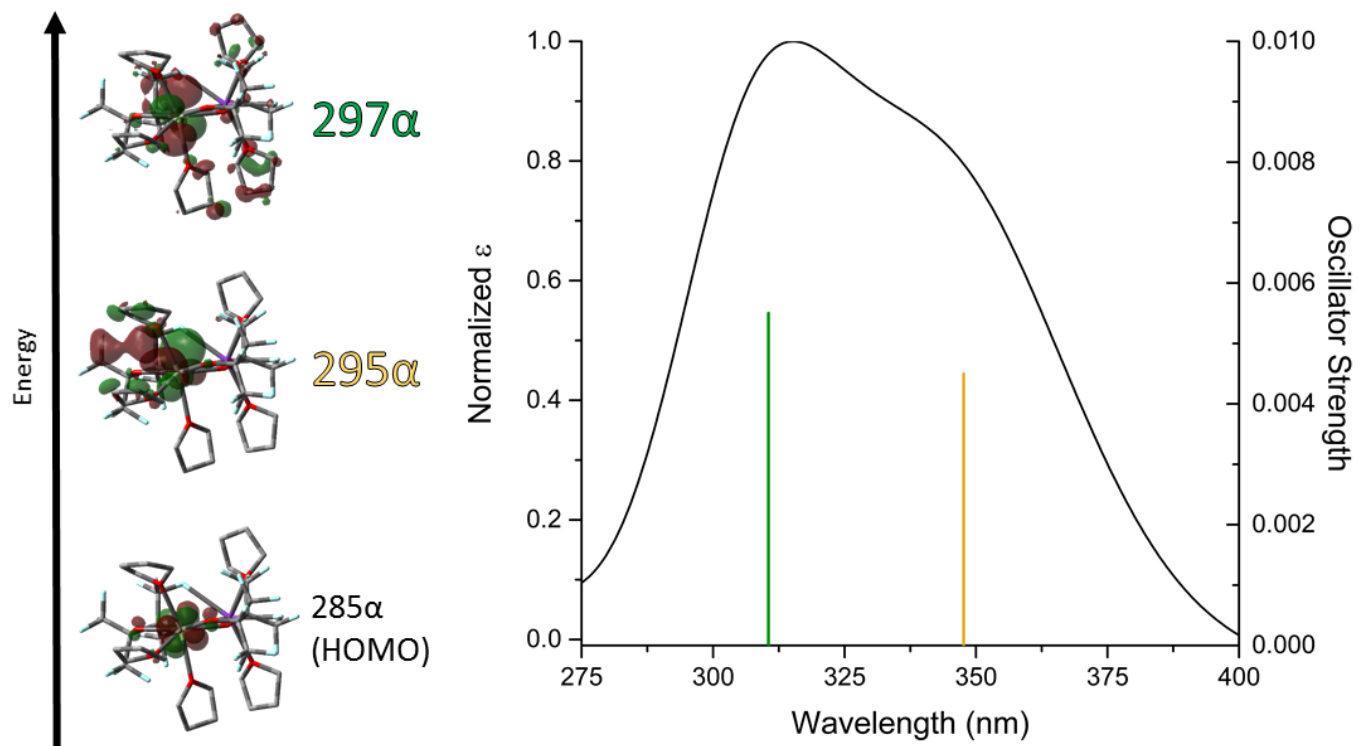
Figure 12. Absorption transitions for **3-Ce** and corresponding donor/acceptor orbitals.
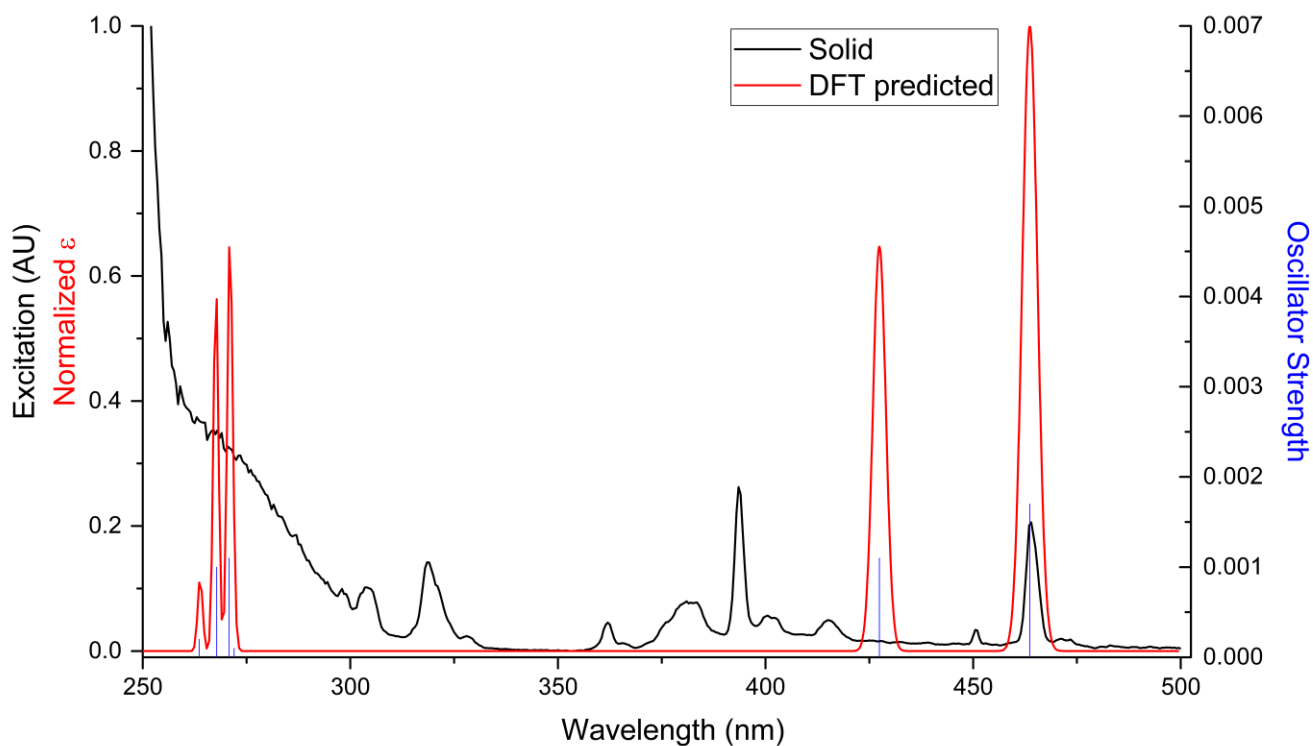
Figure 13. Solid-state excitation (black) and TD-DFT simulated absorption (red) spectra for **2-Eu**, with individual excitations shown in blue. Key excitations in the solid state appear at 395 and 464 nm, with corresponding simulated transitions appearing at 441 and 463 nm.
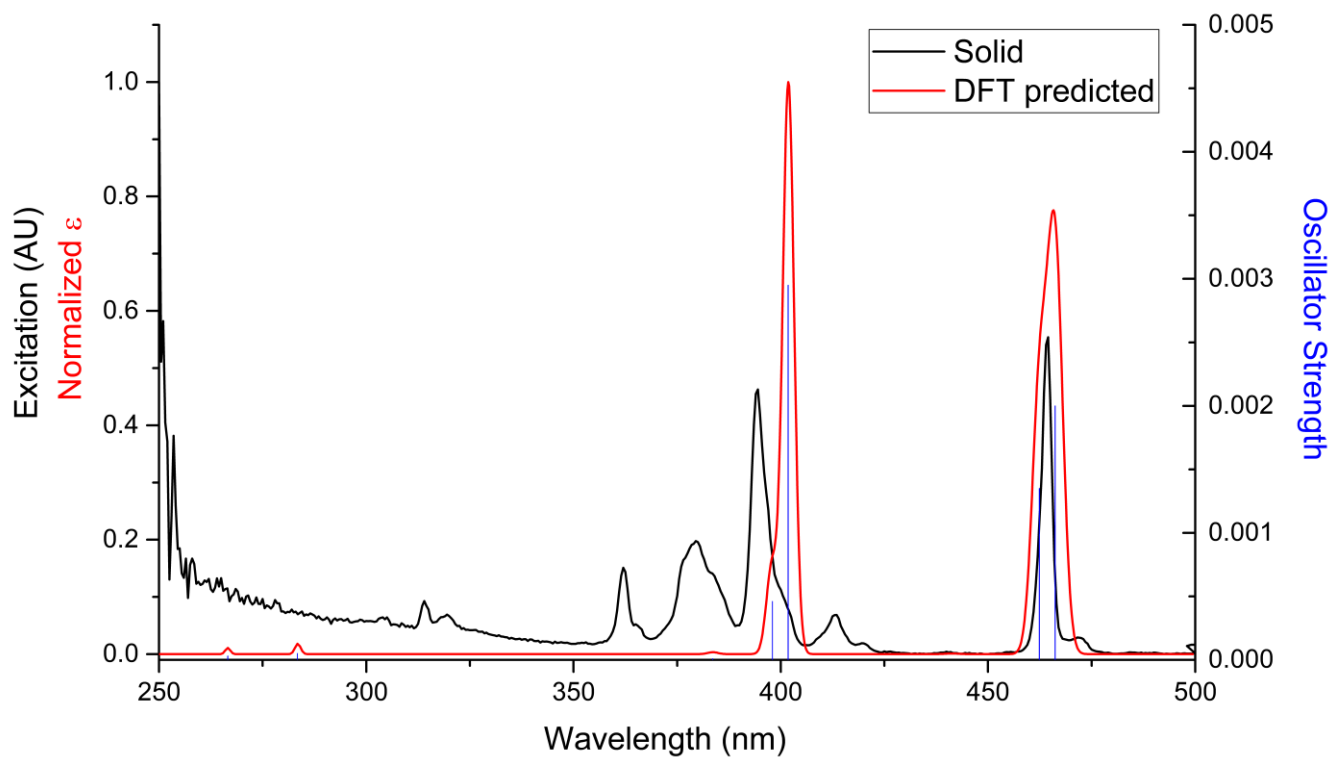
Figure 14. Solid-state excitation (black) and TD-DFT simulated absorption (red) spectra for **4-Eu**, with individual excitations shown in blue. Key excitations in the solid state appear at 395 and 464 nm, with corresponding simulated transitions appearing at 401 and 466 nm.

REFERENCES

1.   de Bettencourt-Dias, A., Lanthanide-based Emitting Materials in Light-emitting Diodes. *Dalton Trans.* **2007,** (22), 2229-2241.

2.   Armelao, L.; Quici, S.; Barigelletti, F.; Accorsi, G.; Bottaro, G.; Cavazzini, M.; Tondello, E., Design of Luminescent Lanthanide Complexes: From Molecules to Highly Efficient Photo-emitting Materials. *Coord. Chem. Rev.* **2010,** *254* (5–6), 487-505.

3.   Eliseeva, S. V.; Bunzli, J.-C. G., Lanthanide luminescence for functional materials and bio-sciences. *Chem. Soc. Rev.* **2010,** *39* (1), 189-227.

4.   Wang, G.; Peng, Q.; Li, Y., Lanthanide-Doped Nanocrystals: Synthesis, Optical-Magnetic Properties, and Applications. *Acc. Chem. Res.* **2011,** *44* (5), 322-332.

5.   Huang, C.-H., *Rare Earth Coordination Chemistry: Fundamentals and Applications*. John Wiley & Sons: 2011.

6.   Hasegawa, Y.; Nakanishi, T., Luminescent Lanthanide Coordination Polymers for Photonic Applications. *RSC Adv.* **2015,** *5* (1), 338-353.

7.   Xu, H.; Cao, C.-S.; Kang, X.-M.; Zhao, B., Lanthanide-based Metal-organic Frameworks as Luminescent Probes. *Dalton Trans.* **2016,** *45* (45), 18003-18017.

8.   Zheng, Y.; Lin, J.; Liang, Y.; Lin, Q.; Yu, Y.; Meng, Q.; Zhou, Y.; Wang, S.; Wang, H.; Zhang, H., A Comparative Study on the Electroluminescence Properties of some Terbium β-diketonate Complexes. *J. Mater. Chem.* **2001,** *11* (10), 2615-2619.

9.   Raj, D. B. A.; Francis, B.; Reddy, M. L. P.; Butorac, R. R.; Lynch, V. M.; Cowley, A. H., Highly Luminescent Poly(Methyl Methacrylate)-Incorporated Europium Complex Supported by a Carbazole-Based Fluorinated β-Diketonate Ligand and a 4,5-Bis(diphenylphosphino)-9,9-dimethylxanthene Oxide Co-Ligand. *Inorg. Chem.* **2010,** *49* (19), 9055-9063.

10.   Ahmed, Z.; Dar, W. A.; Iftikhar, K., Syntheses and Spectroscopic Studies of Volatile Low Symmetry Lanthanide(III) Complexes with Monodentate 1*H*-Indazole and Fluorinated β-diketone. *J. Coord. Chem.* **2012,** *65* (22), 3932-3948.

11.   Hasegawa, Y.; Murakoshi, K.; Wada, Y.; Kim, J.-H.; Nakashima, N.; Yamanaka, T.; Yanagida, S., Characteristic Emission of β-diketonato Nd^{3+} Complexes Dressed with Perfluoroalkyl Groups in DMSO-d6. *Chem. Phys. Lett.* **1996,** *260* (1), 173-177.

12.   Groom, C. R.; Bruno, I. J.; Lightfoot, M. P.; Ward, S. C., The Cambridge Structural Database. *Acta Crystallogr. Sect. B* **2016,** *72* (2), 171-179.

13.   Binnemans, K., *Rare-Earth Beta-Diketonates*. 2005; Vol. 35, p 107-272.

14.   Boyle, T. J.; Ottley, L. A. M., Advances in Structurally Characterized Lanthanide Alkoxide, Aryloxide, and Silyloxide Compounds. *Chem. Rev.* **2008,** *108* (6), 1896-1917.

15.   Lebrun, A.; Namy, J.-L.; Kagan, H. B., A New Preparation of Lanthanide Alkoxide, and Some Applications in Catalysis. *Tetrahedron Lett.* **1991,** *32* (21), 2355-2358.

16.   Anwander, R., Routes to Monomeric Lanthanide Alkoxides. In *Organolanthoid Chemistry: Synthesis, Structure, Catalysis*, Springer Berlin Heidelberg: Berlin, Heidelberg, 1996; pp 149-245.

17.   Boyle, T. J.; Tribby, L. J.; Bunge, S. D., Synthesis and Structural Characterization of a Series of Carboxylic Acid Modified Cerium(III) Alkoxides. *Eur. J. Inorg. Chem.* **2006,** *2006* (22), 4553-4563.

18.   Williams, U. J.; Schneider, D.; Dorfner, W. L.; Maichle-Mossmer, C.; Carroll, P. J.; Anwander, R.; Schelter, E. J., Variation of Electronic Transitions and Reduction Potentials of Cerium(IV) Complexes. *Dalton Trans.* **2014,** *43* (43), 16197-16206.

19.   Buchanan, W. D.; Ruhlandt-Senge, K., M—F Interactions and Heterobimetallics: Furthering the Understanding of Heterobimetallic Stabilization. *Chem. Eur. J.* **2013,** *19* (32), 10708-10715.

20.   Lee, S.; Choi, S.; Park, K. H.; Chae, K. W.; Cho, J. B.; Ahn, Y.; Park, J.-Y.; Koh, K. H., Hot-Filament CVD Synthesis and Application of Carbon Nanostructures. *Thin Solid Films* **2008,** *516* (5), 700-705.

21.   Martin-Ramos, P.; Coya, C.; Lavin, V.; Martin, I. R.; Silva, M. R.; Silva, P. S. P.; Garcia-Velez, M.; Alvarez, A. L.; Martin-Gil, J., Active Layer Solution-Processed NIR-OLEDs Based on Ternary Erbium(III) Complexes with 1,1,1-trifluoro-2,4-pentanedione and Different N,N-donors. *Dalton Trans.* **2014,** *43* (48), 18087-18096.

22.   Martin-Ramos, P.; Silva, M. R.; Coya, C.; Zaldo, C.; Alvarez, A. L.; Alvarez-Garcia, S.; Matos Beja, A. M.; Martin-Gil, J., Novel Erbium(III) Fluorinated β-diketonate Complexes with N,N-donors for Optoelectronics: from Synthesis to Solution-Processed Devices. *J. Mater. Chem. C* **2013,** *1* (15), 2725-2734.

23.   Kogej, K.; Fonseca, S. M.; Rovisco, J.; Azenha, M. E.; Ramos, M. L.; Seixas de Melo, J. S.; Burrows, H. D., Understanding the Interaction between Trivalent Lanthanide Ions and Stereoregular Polymethacrylates through Luminescence, Binding Isotherms, NMR, and Interaction with Cetylpyridinium Chloride. *Langmuir* **2013,** *29* (47), 14429-14437.

24.   Pietrantoni, S.; Francini, R.; Pizzoferrato, R.; Penna, S.; Paolesse, R.; Mandoj, F., Energy Transfer and Excitation Processes in Thin Films of Rare-Earth Organic Complexes for NIR Emission. *Physica Status Solidi (C)* **2007,** *4* (3), 1048-1051.

25.   Norton, K.; Kumar, G. A.; Dilks, J. L.; Emge, T. J.; Riman, R. E.; Brik, M. G.; Brennan, J. G., Lanthanide Compounds with Fluorinated Aryloxide Ligands: Near-Infrared Emission from Nd, Tm, and Er. *Inorg. Chem.* **2009,** *48* (8), 3573-3580.

26.   Tahsini, L.; Specht, S. E.; Lum, J. S.; Nelson, J. J. M.; Long, A. F.; Golen, J. A.; Rheingold, A. L.; Doerrer, L. H., Structural and Electronic Properties of Old and New $A_2[M(pinF)_2]$ Complexes. *Inorg. Chem.* **2013,** *52* (24), 14050-14063.

27.   Hannigan, S. F.; Lum, J. S.; Bacon, J. W.; Moore, C.; Golen, J. A.; Rheingold, A. L.; Doerrer, L. H., Room Temperature Stable Organocuprate Copper(III) Complex. *Organometallics* **2013,** *32* (12), 3429-3436.

28.   Cantalupo, S. A.; Lum, J. S.; Buzzeo, M. C.; Moore, C.; Di Pasquale, A. G.; Rheingold, A. L.; Doerrer, L. H., Three-Coordinate Late Transition Metal Fluorinated Alkoxide Complexes. *Dalton Trans.* **2010,** *39* (2), 374-383.

29.   Cantalupo, S. A.; Fiedler, S. R.; Shores, M. P.; Rheingold, A. L.; Doerrer, L. H., High-Spin Square-Planar Co^{II} and Fe^{II} Complexes and Reasons for Their Electronic Structure. *Angew. Chem., Int. Ed.* **2012,** *51* (Copyright (C) 2012 American Chemical Society (ACS). All Rights Reserved.), 1000-1005.

30.   Cantalupo, S. A.; Ferreira, H. E.; Bataineh, E.; King, A. J.; Petersen, M. V.; Wojtasiewicz, T.; DiPasquale, A. G.; Rheingold, A. L.; Doerrer, L. H., Synthesis with Structural and Electronic Characterization of Homoleptic Fe(II)- and Fe(III)-Fluorinated Phenolate Complexes. *Inorg. Chem.* **2011,** *50* (Copyright (C) 2012 American Chemical Society (ACS). All Rights Reserved.), 6584-6596.

31.   Buzzeo, M. C.; Iqbal, A. H.; Long, C. M.; Millar, D.; Patel, S.; Pellow, M. A.; Saddoughi, S. A.; Smenton, A. L.; Turner, J. F. C.; Wadhawan, J. D.; Compton, R. G.; Golen, J. A.; Rheingold, A. L.; Doerrer, L. H., Homoleptic Cobalt and Copper Phenolate $A_2[M(OAr)_4]$ Compounds: The Effect of Phenoxide Fluorination. *Inorg. Chem.* **2004,** *43* (24), 7709-7725.

32.   Zheng, B. N.; Miranda, M. O.; Di Pasquale, A. G.; Golen, J. A.; Rheingold, A. L.; Doerrer, L. H., Synthesis and Electronic Spectra of Fluorinated Aryloxide and Alkoxide $[NiX_4]^{2-}$ Anions. *Inorg. Chem.* **2009,** *48* (10), 4274-4276.

33.   Lum, J. S.; Tahsini, L.; Golen, J. A.; Moore, C.; Rheingold, A. L.; Doerrer, L. H., K···F/O Interactions Bridge Copper(I) Fluorinated Alkoxide Complexes and Facilitate Dioxygen Activation. *Chem. Eur. J.* **2013,** *19* (20), 6374-6384.

34.   Chen, P. E.; McNeely, J.; Lum, J. S.; Gardner, E. J.; Phillips, V.; Golen, J. A.; Rheingold, A. L.; Doerrer, L. H., LCu(μ-X)₂CuL Compounds: An Induced Cuprophilic Interaction. *Polyhedron* **2016,** *116*, 204-215.

35.   Hannigan, S. F.; Arnoff, A. I.; Neville, S. E.; Lum, J. S.; Golen, J. A.; Rheingold, A. L.; Orth, N.; Ivanović-Burmazović, I.; Liebhäuser, P.; Rösener, T.; Stanek, J.; Hoffmann, A.; Herres-Pawlis, S.; Doerrer, L. H., On the Way to a Trisanionic {Cu$_3$O$_2$} Core for Oxidase Catalysis: Evidence of an Asymmetric Trinuclear Precursor Stabilized by Perfluoropinacolate Ligands. *Chem. Eur. J.* **2017,** *23* (34), 8212-8224.

36.   Lum, J. S.; Chen, P. E.; Rheingold, A. L.; Doerrer, L. H., Zinc(II) Complexes with Fluorinated Monodentate Aryloxide and Alkoxide Ligands. *Polyhedron* **2013,** *58*, 218-228.

37.   Brazeau, S. E. N.; Pope, F.; Huang, V. L.; Anklin, C.; Rheingold, A. L.; Doerrer, L. H., Phosphine Ligands as Protecting Groups for 3d Complexes in Oxidation by O2. *Polyhedron* **2020**, 114609.

38.   Edelmann, F. T., *Synthetic Methods of Organometallics and Inorganic Chemistry*. Thieme Chemistry: Stuttgart, Germany, 1997; Vol. 6.

39.   Frisch, M. J.; Trucks, G. W.; Schlegel, H. B.; Scuseria, G. E.; Robb, M. A.; Cheeseman, J. R.; Scalmani, G.; Barone, V.; Petersson, G. A.; Nakatsuji, H.; Li, X.; Caricato, M.; Marenich, A. V.; Bloino, J.; Janesko, B. G.; Gomperts, R.; Mennucci, B.; Hratchian, H. P.; Ortiz, J. V.; Izmaylov, A. F.; Sonnenberg, J. L.; Williams; Ding, F.; Lipparini, F.; Egidi, F.; Goings, J.; Peng, B.; Petrone, A.; Henderson, T.; Ranasinghe, D.; Zakrzewski, V. G.; Gao, J.; Rega, N.; Zheng, G.; Liang, W.; Hada, M.; Ehara, M.; Toyota, K.; Fukuda, R.; Hasegawa, J.; Ishida, M.; Nakajima, T.; Honda, Y.; Kitao, O.; Nakai, H.; Vreven, T.; Throssell, K.; Montgomery Jr., J. A.; Peralta, J. E.; Ogliaro, F.; Bearpark, M. J.; Heyd, J. J.; Brothers, E. N.; Kudin, K. N.; Staroverov, V. N.; Keith, T. A.; Kobayashi, R.; Normand, J.; Raghavachari, K.; Rendell, A. P.; Burant, J. C.; Iyengar, S. S.; Tomasi, J.; Cossi, M.; Millam, J. M.; Klene, M.; Adamo, C.; Cammi, R.; Ochterski, J. W.; Martin, R. L.; Morokuma, K.; Farkas, O.; Foresman, J. B.; Fox, D. J. *Gaussian 16 Rev. A.03*, Wallingford, CT, 2016.

40.   Cao, X.; Dolg, M., Valence basis sets for relativistic energy-consistent small-core lanthanide pseudopotentials. *The Journal of Chemical Physics* **2001,** *115* (16), 7348-7355.

41.   Feller, D., The role of databases in support of computational chemistry calculations. *J. Comput. Chem.* **1996,** *17* (13), 1571-1586.

42.   Schuchardt, K. L.; Didier, B. T.; Elsethagen, T.; Sun, L.; Gurumoorthi, V.; Chase, J.; Li, J.; Windus, T. L., Basis Set Exchange: A Community Database for Computational Sciences. *Journal of Chemical Information and Modeling* **2007,** *47* (3), 1045-1052.

43.   Andrae, D.; Häußermann, U.; Dolg, M.; Stoll, H.; Preuß, H., Energy-adjustedab initio pseudopotentials for the second and third row transition elements. *Theoretica chimica acta* **1990,** *77* (2), 123-141.

44.   Dennington, R.; Keith, T. A.; Millam, J. M. *GaussView Version 6*, Semichem Inc.: Shawnee Mission, KS, 2016.

45.   Andrienko, G. A. *ChemCraft*, 1.8 (Build 523a).

46.   Glendening, E. D.; Badenhoop, J. K.; Reed, A. E.; Carpenter, J. E.; Bohmann, J. A.; Morales, C. M.; Landis, C. R.; Weinhold, F. *NBO 6.0*, Theoretical Chemistry Institute, University of Wisconsin, Madison, 2013.

47.   Glendening, E. D.; Landis, C. R.; Weinhold, F., NBO 6.0: Natural bond orbital analysis program. *J. Comput. Chem.* **2013,** *34* (16), 1429-1437.

48.   Fonseca Guerra, C.; Snijders, G. J.; te Velde, G.; Baerends, J. E., Towards an Order-N DFT Method. *Theor. Chem. Acc.* **1998,** *99* (6), 391-403.

49.   te Velde, G.; Bickelhaupt, F. M.; Baerends, E. J.; Fonseca Guerra, C.; van Gisbergen, S. J. A.; Snijders, J. G.; Ziegler, T., Chemistry with ADF. *J. Comput. Chem.* **2001,** *22* (9), 931-967.

50.   Neese, F., The ORCA program system. *Wiley Interdisciplinary Reviews: Computational Molecular Science* **2012,** *2* (1), 73-78.

51.   Neese, F., *ORCA – An Ab Initio, DFT and Semiempirical SCF-MO Package, Ver. 4.0*. Max Planck Institute for Chemical Energy Conversion: Mülheim a. d. Rurh, Germany, 2017.

52.   Neese, F., Software update: the ORCA program system, version 4.0. *Wiley Interdisciplinary Reviews: Computational Molecular Science* **2018,** *8* (1), e1327.

53.   Aravena, D.; Atanasov, M.; Neese, F., Periodic Trends in Lanthanide Compounds through the Eyes of Multireference ab Initio Theory. *Inorg. Chem.* **2016,** *55* (9), 4457-4469.

54.   Weigend, F.; Ahlrichs, R., Balanced basis sets of split valence, triple zeta valence and quadruple zeta valence quality for H to Rn: Design and assessment of accuracy. *Physical Chemistry Chemical Physics* **2005,** *7* (18), 3297-3305.

55.   Nakajima, T.; Hirao, K., The Douglas–Kroll–Hess Approach. *Chem. Rev.* **2012,** *112* (1), 385-402.

56.   Ganyushin, D.; Neese, F., First-principles calculations of zero-field splitting parameters. *The Journal of Chemical Physics* **2006,** *125* (2), 024103.

57.   Jung, J.; Atanasov, M.; Neese, F., Ab Initio Ligand-Field Theory Analysis and Covalency Trends in Actinide and Lanthanide Free Ions and Octahedral Complexes. *Inorg. Chem.* **2017,** *56* (15), 8802-8816.

58.   Freidzon, A. Y.; Kurbatov, I. A.; Vovna, V. I., Ab initio calculation of energy levels of trivalent lanthanide ions. *Physical Chemistry Chemical Physics* **2018,** *20* (21), 14564-14577.

59.   Angeli, C.; Cimiraglia, R.; Malrieu, J.-P., N-electron valence state perturbation theory: a fast implementation of the strongly contracted variant. *Chem. Phys. Lett.* **2001,** *350* (3), 297-305.

60.   Angeli, C.; Cimiraglia, R.; Evangelisti, S.; Leininger, T.; Malrieu, J. P., Introduction of n-electron valence states for multireference perturbation theory. *The Journal of Chemical Physics* **2001,** *114* (23), 10252-10264.

61.   Angeli, C.; Bories, B.; Cavallini, A.; Cimiraglia, R., Third-order multireference perturbation theory: The n-electron valence state perturbation-theory approach. *The Journal of Chemical Physics* **2006,** *124* (5), 054108.

62.   Neese, F., A spectroscopy oriented configuration interaction procedure. *The Journal of Chemical Physics* **2003,** *119* (18), 9428-9443.

63.   Peterson, K. A.; Figgen, D.; Dolg, M.; Stoll, H., Energy-consistent relativistic pseudopotentials and correlation consistent basis sets for the 4d elements Y–Pd. *The Journal of Chemical Physics* **2007,** *126* (12), 124101.

64.   Gradeff, P. S.; Yunlu, K.; Deming, T. J.; Olofson, J. M.; Doedens, R. J.; Evans, W. J., Synthesis of yttrium and lanthanide silyloxy complexes from anhydrous nitrate and oxo alkoxide precursors and the x-ray crystal structure of [Ce(OSiPh$_3$)$_3$(THF)$_3$](THF). *Inorg. Chem.* **1990,** *29* (3), 420-424.

65.   Robinson, J. R.; Carroll, P. J.; Walsh, P. J.; Schelter, E. J., The Impact of Ligand Reorganization on Cerium(III) Oxidation Chemistry. *Angew. Chem. Int. Ed.* **2012,** *51* (40), 10159-10163.

66.   Robinson, J. R.; Booth, C. H.; Carroll, P. J.; Walsh, P. J.; Schelter, E. J., Dimeric Rare-Earth BINOLate Complexes: Activation of 1,4-Benzoquinone through Lewis Acid Promoted Potential Shifts. *Chem. Eur. J.* **2013,** *19* (19), 5996-6004.

67.   Rukk, N. S.; Albov, D. V.; Shamsiev, R. S.; Mudretsova, S. N.; Davydova, G. A.; Sadikov, G. G.; Antsyshkina, A. S.; Kravchenko, V. V.; Skryabina, A. Y.; Apryshko, G. N.; Zamalyutin, V. V.; Mironova, E. A., Synthesis, X-ray Crystal Structure and Cytotoxicity Studies of Lanthanide(III) Iodide Complexes with Antipyrine. *Polyhedron* **2012,** *44* (1), 124-132.

68.   Mahoney, B. D.; Piro, N. A.; Carroll, P. J.; Schelter, E. J., Synthesis, Electrochemistry, and Reactivity of Cerium(III/IV) Methylene-Bis-Phenolate Complexes. *Inorg. Chem.* **2013,** *52* (10), 5970-5977.

69.   Levin, J. R.; Gu, J.; Carroll, P. J.; Schelter, E. J., Lanthanide(III) 2-naphthoxide Complexes Stabilized by Interligand Non-covalent Interactions. *Dalton Trans.* **2012,** *41* (26), 7870-7872.

70.   Robinson, J. R.; Qiao, Y.; Gu, J.; Carroll, P. J.; Walsh, P. J.; Schelter, E. J., The Role of Dynamic Ligand Exchange in the Oxidation Chemistry of Cerium(III). *Chem. Sci.* **2016,** *7* (7), 4537-4547.

71.   Arnold, P. L.; Liddle, S. T., Centre, T. C. C. D., Ed. 2006.

72.   Bienfait, A. M.; Schädle, C.; Maichle-Mössmer, C.; Törnroos, K. W.; Anwander, R., Europium bis(dimethylsilyl)amides including mixed-valent Eu3[N(SiHMe2)2]6[μ-N(SiHMe2)2]2. *Dalton Trans.* **2014,** *43* (46), 17324-17332.

73.   Bienfait, A. M.; Wolf, B. M.; Törnroos, K. W.; Anwander, R., Trivalent Rare-Earth-Metal Bis(trimethylsilyl)amide Halide Complexes by Targeted Oxidations. *Inorg. Chem.* **2018,** *57* (9), 5204-5212.

74.   de Bruin-Dickason, C. N.; Boutland, A. J.; Dange, D.; Deacon, G. B.; Jones, C., Redox transmetallation approaches to the synthesis of extremely bulky amido-lanthanoid(ii) and -calcium(ii) complexes. *Dalton Trans.* **2018,** *47* (28), 9512-9520.

75.   Deacon, G. B.; Junk, P. C.; Moxey, G. J., Metal–π Interactions Dominate in the Solid-State Structures of Molecular Heterobimetallic Alkali-Metal–Europium(II) Aryloxo Complexes. *Chemistry – An Asian Journal* **2009,** *4* (8), 1309-1317.

76.   Feng, Z.; Wei, Y.; Zhou, S.; Zhang, G.; Zhu, X.; Guo, L.; Wang, S.; Mu, X., Reactivity of functionalized indoles with rare-earth metal amides. Synthesis, characterization and catalytic activity of rare-earth metal complexes incorporating indolyl ligands. *Dalton Trans.* **2015,** *44* (47), 20502-20513.

77.   Gröb, T.; Seybert, G.; Massa, W.; Harms, K.; Dehnicke, K., Die Reaktionen von Europium und Yttrium mit N-Iod-triphenylphosphanimin. Kristallstrukturen von [EuI2(DME)3], [Eu2I(NPPh3)5(DME)] und [Y2I(NPPh3)4(THF)4]+I3–. *Z. Anorg. Allg. Chem.* **2000,** *626* (6), 1361-1366.

78.   Heckmann, G.; Niemeyer, M., Synthesis and First Structural Characterization of Lanthanide(II) Aryls: Observation of a Schlenk Equilibrium in Europium(II) and Ytterbium(II) Chemistry. *Journal of the American Chemical Society* **2000,** *122* (17), 4227-4228.

79.   Heitmann, D.; Jones, C.; Junk, P. C.; Lippert, K.-A.; Stasch, A., Homoleptic lanthanide(ii)–bis(guanidinate) complexes, [Ln(Giso)2] (Giso = [(ArN)2CN(C6H11)2]−, Ar = C6H3Pri2-2,6): planar 4-coordinate (Ln = Sm or Eu) vs distorted tetrahedral (Ln = Yb) geometries. *Dalton Trans.* **2007,** (2), 187-189.

80.   Heitmann, D.; Jones, C.; Mills, D. P.; Stasch, A., Low coordinate lanthanide(ii) complexes supported by bulky guanidinato and amidinato ligands. *Dalton Trans.* **2010,** *39* (7), 1877-1882.

81.   Jiang, Y.; Zhu, X.; Chen, M.; Wang, Y.; Yao, Y.; Wu, B.; Shen, Q., Synthesis and Structural Characterization of Mixed-Valent Ytterbium and Europium Complexes Supported by a Phenoxy(quinolinyl)amide Ligand. *Organometallics* **2014,** *33* (8), 1972-1976.

82.   Just, O.; Rees, W. S., Synthesis and Single-Crystal X-ray Diffraction Examination of a Structurally Homologous Series of Tetracoordinate Heteroleptic Anionic Lanthanide Complexes: Ln{N[Si(CH3)2CH2CH2Si(CH3)2]}3(μ-Cl)Li(L)3 [Ln = Sm, Eu, Gd, Tb, Dy, Ho, Er, Tm, Yb; (L)3 = (THF)3, (Et2O)3, (THF)2(Et2O)]. *Inorg. Chem.* **2001,** *40* (8), 1751-1755.

83.   Li, W.; Zhang, Z.; Yao, Y.; Zhang, Y.; Shen, Q., Control of Conformations of Piperazidine-Bridged Bis(phenolato) Groups: Syntheses and Structures of Bimetallic and Monometallic Lanthanide Amides and Their Application in the Polymerization of Lactides. *Organometallics* **2012,** *31* (9), 3499-3511.

84.   Pan, C.-L.; Pan, Y.-S.; Wang, J.; Song, J.-F., A heterometallic sandwich complex of europium(ii) for luminescent studies. *Dalton Trans.* **2011,** *40* (24), 6361-6363.

85.   Rabe, G. W.; Yap, G. P. A.; Rheingold, A. L., Lanthanide Phosphido Complexes: A Comparison of the Divalent Homoleptic Species Ln[(μ-PtBu2)2Li(thf)]2 (Ln = Yb, Eu, Sm) Including the Structural Characterization and a Europium-151 Mössbauer Spectrum of Eu[(μ-PtBu2)2Li(thf)]21. *Inorg. Chem.* **1997,** *36* (15), 3212-3215.

86.   Shen, X.; Zhang, Y.; Xue, M.; Shen, Q., Reduction of Sterically Hindered β-Diketiminato Europium(iii) Complexes by the β-Diketiminato Anion: A Convenient Route for the Synthesis of β-Diketiminato Europium(ii) Complexes. *Dalton Trans.* **2012,** *41* (13), 3668-3674.

87.   Wolf, B. M.; Stuhl, C.; Anwander, R., Synthesis of homometallic divalent lanthanide organoimides from benzyl complexes. *Chem. Commun.* **2018,** *54* (64), 8826-8829.

88.   Zhou, S.-L.; Wang, S.-W.; Yang, G.-S.; Liu, X.-Y.; Sheng, E.-H.; Zhang, K.-H.; Cheng, L.; Huang, Z.-X., Synthesis, structure, and catalytic activity of tetracoordinate lanthanide amides [(Me3Si)2N]3Ln(μ-Cl)Li(THF)3 (Ln=Nd, Sm, Eu). *Polyhedron* **2003,** *22* (7), 1019-1024.

89.   Zhu, X.; Wang, S.; Zhou, S.; Wei, Y.; Zhang, L.; Wang, F.; Feng, Z.; Guo, L.; Mu, X., Lanthanide Amido Complexes Incorporating Amino-Coordinate-Lithium Bridged Bis(indolyl) Ligands: Synthesis, Characterization, and Catalysis for Hydrophosphonylation of Aldehydes and Aldimines. *Inorg. Chem.* **2012,** *51* (13), 7134-7143.

90.   Aspinall, H. C.; Bradley, D. C.; Hursthouse, M. B.; Sales, K. D.; Walker, N. P. C., Lanthanide thiolate complexes; synthesis of [Ln{N(SiMe3)2}(μ-SBut)]2(Ln = Eu, Gd, Y) and the X-ray crystal structure of the Gd complex. *J. Chem. Soc., Chem. Commun.* **1985,** (22), 1585-1586.

91.   Freeman, G. E.; Raymond, K. N., Specific sequestering agents for the actinides. 12. Synthetic and structural chemistry of gadolinium and holmium catecholates. *Inorg. Chem.* **1985,** *24* (9), 1410-1417.

92.   Hatanpää, T.; Kukli, K.; Ritala, M.; Leskelä, M., Crystal structures and thermal properties of some rare earth alkoxides with tertiary alcohols. *J. Therm. Anal. Calorim.* **2011,** *105* (1), 61.

93.   Karl, M.; Harms, K.; Dehnicke, K., Synthese und Kristallstrukturen der Natrium–Amido-Metallate [(THF)2Na(Ph2N)2Ln{N(SiMe3)2}2] mit Ln = Gd und Yb. *Z. Anorg. Allg. Chem.* **1999,** *625* (11), 1774-1776.

94.   Liu, P.; Chen, H.; Zhang, Y.; Xue, M.; Yao, Y.; Shen, Q., Synthesis of γ-amidine-functionalized dianionic β-diketiminato lanthanide amides and trianionic β-diketiminato Na/Sm heterobimetallic complexes and their reactivity in polymerization of l-lactide. *Dalton Trans.* **2014,** *43* (14), 5586-5594.

95.   Trambitas, A. G.; Panda, T. K.; Jenter, J.; Roesky, P. W.; Daniliuc, C.; Hrib, C. G.; Jones, P. G.; Tamm, M., Rare-Earth Metal Alkyl, Amido, and Cyclopentadienyl Complexes Supported by Imidazolin-2-iminato Ligands: Synthesis, Structural Characterization, and Catalytic Application. *Inorg. Chem.* **2010,** *49* (5), 2435-2446.

96.   Zhao, W.; Wang, C.; Zhang, Y.; Zhang, Y.; Xue, S.; Tao, Z.; Clegg, J. K.; Zhu, Q.; Lindoy, L. F.; Wei, G., Adducts of aqua complexes of Ln3+ with hexahydroxyhexamethylcucurbit[6]uril: potential application in the isolation of heavy lanthanides. *New J. Chem.* **2016,** *40* (3), 2763-2767.

97.   Boyle, T. J.; Bunge, S. D.; Clem, P. G.; Richardson, J.; Dawley, J. T.; Ottley, L. A. M.; Rodriguez, M. A.; Tuttle, B. A.; Avilucea, G. R.; Tissot, R. G., Synthesis and Characterization of a Family of Structurally Characterized Dysprosium Alkoxides for Improved Fatigue-Resistance Characteristics of PDyZT Thin Films. *Inorg. Chem.* **2005,** *44* (5), 1588-1600.

98.   Dickie, C. M.; Laughlin, A. L.; Wofford, J. D.; Bhuvanesh, N. S.; Nippe, M., Transition metal redox switches for reversible "on/off" and "slow/fast" single-molecule magnet behaviour in dysprosium and erbium bis-diamidoferrocene complexes. *Chem. Sci.* **2017,** *8* (12), 8039-8049.

99.   Fieser, M. E.; Palumbo, C. T.; La Pierre, H. S.; Halter, D. P.; Voora, V. K.; Ziller, J. W.; Furche, F.; Meyer, K.; Evans, W. J., Comparisons of lanthanide/actinide +2 ions in a tris(aryloxide)arene coordination environment. *Chem. Sci.* **2017,** *8* (11), 7424-7433.

100.   Long, J.; Shestakov, B. G.; Liu, D.; Chibotaru, L. F.; Guari, Y.; Cherkasov, A. V.; Fukin, G. K.; Trifonov, A. A.; Larionova, J., An organolanthanide(iii) single-molecule magnet with an axial crystal-field: influence of the Raman process over the slow relaxation. *Chem. Commun.* **2017,** *53* (34), 4706-4709.

101.   Steele, L. A. M.; Boyle, T. J.; Kemp, R. A.; Moore, C., The selective insertion of carbon dioxide into a lanthanide(III) 2,6-di-t-butyl-phenoxide bond. *Polyhedron* **2012,** *42* (1), 258-264.

102.   Wu, Y.; Wang, S.; Zhu, X.; Yang, G.; Wei, Y.; Zhang, L.; Song, H.-b., Synthesis, Characterization, and Catalytic Activity of Rare Earth Metal Amides Supported by a Diamido Ligand with a CH2SiMe2 Link. *Inorg. Chem.* **2008,** *47* (12), 5503-5511.

103.   Yang, S.; Zhu, X.; Zhou, S.; Wang, S.; Feng, Z.; Wei, Y.; Miao, H.; Guo, L.; Wang, F.; Zhang, G.; Gu, X.; Mu, X., Synthesis, structure, and catalytic activity of novel trinuclear rare-earth metal amido complexes incorporating μ–η5:η1 bonding indolyl and μ3-oxo groups. *Dalton Trans.* **2014,** *43* (6), 2521-2533.

104.   Yu, K.-X.; Ding, Y.-S.; Han, T.; Leng, J.-D.; Zheng, Y.-Z., Magnetic relaxations in four-coordinate Dy(iii) complexes: effects of anionic surroundings and short Dy–O bonds. *Inorganic Chemistry Frontiers* **2016,** *3* (8), 1028-1034.

105.   Yuan, Q.; Zhou, S.; Zhu, X.; Wei, Y.; Wang, S.; Mu, X.; Yao, F.; Zhang, G.; Chen, Z., Heterometallic rare-earth metal complexes with imino-functionalized 8-hydroxyquinolyl ligands: synthesis, characterization and catalytic activity towards hydrophosphinylation of trans-β-nitroalkene. *New J. Chem.* **2015,** *39* (10), 7626-7632.

106.   Zhang, G.; Deng, B.; Wang, S.; Wei, Y.; Zhou, S.; Zhu, X.; Huang, Z.; Mu, X., Di and trinuclear rare-earth metal complexes supported by 3-amido appended indolyl ligands: synthesis, characterization and catalytic activity towards isoprene 1,4-cis polymerization. *Dalton Trans.* **2016,** *45* (39), 15445-15456.

107.   Zhang, P.; Jung, J.; Zhang, L.; Tang, J.; Le Guennic, B., Elucidating the Magnetic Anisotropy and Relaxation Dynamics of Low-Coordinate Lanthanide Compounds. *Inorg. Chem.* **2016,** *55* (4), 1905-1911.

108.   Zhu, X.; Li, Y.; Wei, Y.; Wang, S.; Zhou, S.; Zhang, L., Reactivity of 3-Imino-Functionalized Indoles with Rare-Earth-Metal Amides: Unexpected Substituent Effects on C–H Activation Pathways and Assembly of Rare-Earth-Metal Complexes. *Organometallics* **2016,** *35* (11), 1838-1846.

109.   Mishra, S.; Daniele, S., Metal–Organic Derivatives with Fluorinated Ligands as Precursors for Inorganic Nanomaterials. *Chem. Rev.* **2015,** *115* (16), 8379-8448.

110.   Buchanan, W. D.; Guino-o, M. A.; Ruhlandt-Senge, K., Highly Volatile Alkaline Earth Metal Fluoroalkoxides. *Inorg. Chem.* **2010,** *49* (15), 7144-7155.

111.   Allen, F. H.; Kennard, O.; Watson, D. G.; Brammer, L.; Orpen, A. G.; Taylor, R., Tables of bond lengths determined by x-ray and neutron diffraction. Part 1. Bond lengths in organic compounds. *J. Chem. Soc., Perkin Trans. 2* **1987,** (12), S1-S19.

112.   Kotyk, C. M.; MacDonald, M. R.; Ziller, J. W.; Evans, W. J., Reactivity of the Ln2+ Complexes [K(2.2.2-cryptand)][(C5H4SiMe3)3Ln]: Reduction of Naphthalene and Biphenyl. *Organometallics* **2015,** *34* (11), 2287-2295.

113.   Ellis, R. J.; Meridiano, Y.; Chiarizia, R.; Berthon, L.; Muller, J.; Couston, L.; Antonio, M. R., Periodic Behavior of Lanthanide Coordination within Reverse Micelles. *Chem. Eur. J.* **2013,** *19* (8), 2663-2675.

114.   Lundberg, D.; Persson, I.; Eriksson, L.; D'Angelo, P.; De Panfilis, S., Structural Study of the N,N′-Dimethylpropyleneurea Solvated Lanthanoid(III) Ions in Solution and Solid State with an Analysis of the Ionic Radii of Lanthanoid(III) Ions. *Inorg. Chem.* **2010,** *49* (10), 4420-4432.

115.   Raymond, K. N.; Wellman, D. L.; Sgarlata, C.; Hill, A. P., Curvature of the lanthanide contraction: An explanation. *Comptes Rendus Chimie* **2010,** *13* (6), 849-852.

116.   Gagne, O. C., Bond-length distributions for ions bonded to oxygen: results for the lanthanides and actinides and discussion of the f-block contraction. *Acta Crystallogr. Sect. B* **2018,** *74* (1), 49-62.

117.   Shannon, R. D., Revised effective ionic radii and systematic studies of interatomic distances in halides and chalcogenides. *Acta Crystallogr., Sect. A* **1976,** *A32* (5), 751-67.

118.   Robinson, J. R.; Gordon, Z.; Booth, C. H.; Carroll, P. J.; Walsh, P. J.; Schelter, E. J., Tuning Reactivity and Electronic Properties through Ligand Reorganization within a Cerium Heterobimetallic Framework. *Journal of the American Chemical Society* **2013,** *135* (50), 19016-19024.

119.   Katkova, M. A.; Burin, M. E.; Logunov, A. A.; Ilichev, V. A.; Konev, A. N.; Fukin, G. K.; Bochkarev, M. N., Lanthanide Imidodiphosphinate Complexes: Synthesis, Structure and New Aspects of Electroluminescent Properties. *Synth. Met.* **2009,** *159* (14), 1398-1402.

120.   Berthet, J.-C.; Nierlich, M.; Ephritikhine, M., A Comparison of Analogous 4*f*- and 5*f*-Element Compounds: Syntheses and Crystal Structures of Triphenylphosphine Oxide Complexes of Lanthanide(III) and Uranium(III) Triflates and Iodides [MX2(OPPh3)4][X] (X=OTf and M=Ce or U; X=I and M=Nd, Ce, La, U). *Polyhedron* **2003,** *22* (27), 3475-3482.

121.   Hamidi, S.; Deacon, G. B.; Junk, P. C.; Neumann, P., Direct reaction of iodine-activated lanthanoid metals with 2,6-diisopropylphenol. *Dalton Trans.* **2012,** *41* (12), 3541-3552.

122.   Xu, X.; Ma, M.; Yao, Y.; Zhang, Y.; Shen, Q., Synthesis, Characterisation of Carbon-Bridged (Diphenolato)lanthanide Complexes and Their Catalytic Activity for Diels–Alder Reactions. *Eur. J. Inorg. Chem.* **2005,** *2005* (4), 676-684.

123.   Diamantopoulou, E.; Papaefstathiou, G. S.; Terzis, A.; Raptopoulou, C. P.; Desseyn, H. O.; Perlepes, S. P., Hydrogen bonded networks based on lanthanide(III) complexes of N,N′-dimethylurea (DMU): preparation, characterisation, and crystal structures of [Nd(DMU)6][NdCl6] and [Nd(NO3)3(DMU)3]. *Polyhedron* **2003,** *22* (6), 825-835.

124.   Evans, W. J.; Ansari, M. A.; Ziller, J. W., Isolation and structural characterization of tetra- and pentaheterometallic neodymium 4-methylphenoxide complexes. *Polyhedron* **1997,** *16* (19), 3429-3434.

125.   Glover, P. B.; Bassett, A. P.; Nockemann, P.; Kariuki, B. M.; Van Deun, R.; Pikramenou, Z., Fully Fluorinated Imidodiphosphinate Shells for Visible- and NIR-Emitting Lanthanides: Hitherto Unexpected Effects of Sensitizer Fluorination on Lanthanide Emission Properties. *Chem. Eur. J.* **2007,** *13* (22), 6308-6320.

126.   Sasai, H.; Suzuki, T.; Itoh, N.; Tanaka, K.; Date, T.; Okamura, K.; Shibasaki, M., Catalytic asymmetric nitroaldol reaction using optically active rare earth BINOL complexes: investigation of the catalyst structure. *Journal of the American Chemical Society* **1993,** *115* (22), 10372-10373.

127.   Fawcett, J.; Platt, A. W. G.; Russell, D. R., Structures and catalytic properties of triphenylphosphine oxide complexes of scandium and lanthanide triflates. *Polyhedron* **2002,** *21* (3), 287-293.

128.   Gupta, S. K.; Rajeshkumar, T.; Rajaraman, G.; Murugavel, R., An unprecedented zero field neodymium(III) single-ion magnet based on a phosphonic diamide. *Chem. Commun.* **2016,** *52* (44), 7168-7171.

129.   Veith, M.; Mathur, S.; Lecerf, N.; Bartz, K.; Heintz, M.; Huch, V., Synthesis of a $NdAlO_3/Al_2O_3$ Ceramic−Ceramic Composite by Single-Source Precursor CVD. *Chem. Mater.* **2000,** *12* (2), 271-274.

130.   Clark, L.; Deacon, G. B.; Forsyth, C. M.; Junk, P. C.; Mountford, P.; Townley, J. P., Low-coordinate rare-earth complexes of the asymmetric 2,4-di-tert-butylphenolate ligand prepared by redoxtransmetallation/protolysis reactions, and their reactivity towards ring-opening polymerisation. *Dalton Trans.* **2010,** *39* (29), 6693-6704.

131.   Arndt, S.; Beckerle, K.; Zeimentz, P. M.; Spaniol, T. P.; Okuda, J., Cationic Yttrium Methyl Complexes as Functional Models for Polymerization Catalysts of 1,3-Dienes. *Angew. Chem. Int. Ed.* **2005,** *44* (45), 7473-7477.

132.   Kuzyaev, D. M.; Balashova, T. V.; Burin, M. E.; Fukin, G. K.; Rumyantcev, R. V.; Pushkarev, A. P.; Ilichev, V. A.; Grishin, I. D.; Vorozhtsov, D. L.; Bochkarev, M. N., Synthesis, Structure and Luminescent Properties of Lanthanide Fluoroalkoxides. *Dalton Trans.* **2016,** *45* (8), 3464-3472.

133.   Bünzli, J.-C. G., On the Design of Highly Luminescent Lanthanide Complexes. *Coord. Chem. Rev.* **2015,** *293*, 19-47.

134.   de Bettencourt-Dias, A., Introduction to Lanthanide Ion Luminescence. In *Luminescence of Lanthanide Ions in Coordination Compounds and Nanomaterials*, 1st ed.; de Bettencourt-Dias, A., Ed. John Wiley & Sons, Ltd.: Somerset, GB, 2014; pp 1-48.

135.   Hazin, P. N.; Lakshminarayan, C.; Brinen, L. S.; Knee, J. L.; Bruno, J. W.; Streib, W. E.; Folting, K., Luminescence Spectra and Lifetimes of Cerium(III) Compounds as Indicators of Solution Behavior and Radiative Efficiency. *Inorg. Chem.* **1988,** *27* (8), 1393-1400.

136.   Yin, H.; Jin, Y.; Hertzog, J. E.; Mullane, K. C.; Carroll, P. J.; Manor, B. C.; Anna, J. M.; Schelter, E. J., The Hexachlorocerate(III) Anion: A Potent, Benchtop Stable, and Readily Available Ultraviolet A Photosensitizer for Aryl Chlorides. *Journal of the American Chemical Society* **2016,** *138* (50), 16266-16273.

137.   Tanner, P. A., Lanthanide Luminescence in Solids. In *Lanthanide Luminescence: Photophysical, Analytical and Biological Aspects*, Hänninen, P.; Härmä, H., Eds. Springer: Berlin, 2011; pp 183-233.

138.   Carnall, W. T.; Crosswhite, H.; Crosswhite, H. M. *Energy Level Structure and Transition Probabilities in the Spectra of the Trivalent Lanthanides in LaF_3*; Argonne National Laboratory: Argonne, 1977.

139.   Wang, J.; Deng, R.; MacDonald, M. A.; Chen, B.; Yuan, J.; Wang, F.; Chi, D.; Andy Hor, T. S.; Zhang, P.; Liu, G.; Han, Y.; Liu, X., Enhancing multiphoton upconversion through energy clustering at sublattice level. *Nature Materials* **2014,** *13* (2), 157-162.

140.   Cui, Y.; Fan, X.; Hong, Z.; Wang, M., Synthesis and Luminescence Properties of Lanthanide (III)-Doped YF3 Nanoparticles. *Journal of Nanoscience and Nanotechnology* **2006,** *6* (3), 830-836.

141.   Mascetti, J.; Fouassier, C.; Hagenmuller, P., Concentration quenching of the Nd3+ emission in alkali rare earth borates. *J. Solid State Chem.* **1983,** *50* (2), 204-212.